SCHOOL OF
ENGINEERING AND DESIGN

TECHNISCHE UNIVERSITÄT MÜNCHEN

Bachelor's Thesis in Mechanical Engineering

Direct imaging of high-intensity positron beams with CMOS sensors

Michael Berghold

SCHOOL OF
ENGINEERING AND DESIGN

TECHNISCHE UNIVERSITÄT MÜNCHEN

Bachelor's Thesis in Mechanical Engineering

Direct imaging of high-intensity positron beams with CMOS sensors

Direkte Abbildung von Positronenstrahlen hoher Intensität mit CMOS sensoren

Author:	Michael Berghold
Supervisor:	Prof. Dr. Rudolf Neu
Advisor:	Dr. Francesco Guatieri
Submission Date:	22. 11. 2022

Abstract

A whole range of powerful techniques available to material scientists today employ the use of positions. Most modern positron-based techniques require the production of a focused low-energy beam.

Of fundamental importance to achieve a sharply focused positron beam is the ability to measure the beam's cross section at the desired focal point. Since determining the optimal currents and voltages to be applied to the focusing elements is an iterative process steered by optimizing algorithms, the time required to focus a positron beam heavily depends on the speed of both the beam monitoring and field adjustment. Using state of the art technology, beam focusing at the NEPOMUC beamline at FRM II usually requires hours to complete [1].

In this thesis a novel approach to imaging the cross section of a positron beam was investigated, with the ultimate goal of superseding the current methods in speed and resolution. The proposed design is based on the use of commercial image sensors, such as they are found in smartphones and webcams. Specifically, the sensors in question are of the type employing complementary metal-oxide semiconductors (CMOS) to amplify a photo-generated charge – such sensors are, today, ubiquitous and affordable.

The tests performed on commercially available sensors confirmed their viability as positron detectors, with performances that exceed, on specific metrics, that of specialized equipment. Specifically, sensors that were modified by coating them with a thin layer of phosphor showed the capability to image positron beams having very low implantation energies, as long as the beam emittance exceeds 350 positrons/s/mm^2 at the sensor surface, with a lateral resolution of 10 µm. Sensors that were modified by removing their microlens array and color filter were shown to be able to detect single positrons having a kinetic energy in excess of 5.5 keV, with an efficiency close to 100% and a lateral resolution below 1 µm.

These results are extremely promising and demonstrate the potential of modern integrated imaging sensors as positron detector devices.

Contents

1 Introduction

Measurement of the shape and intensity of the particle beam is an essential requirement to the effective operation of a low-energy positron beam. A variety of methods have been developed to measure the position, shape and intensity of a positron beam - chief amongst which are the use of Micro Channel Plates (MCPs) [2–4] and the so-called "knife-edge" method [1, 5].

In an MCP, the incoming positrons are first converted into electrons and subsequently amplified and accelerated [6] before being captured by a phosphor screen and converted into light. The screen is then imaged by a camera system, typically placed outside of the vacuum chamber. Despite this imaging technique being both powerful and well-established, it is not ubiquitously used due to its demanding operational requirements.

While MCP detectors can be manufactured to accommodate a wide range of setups, their resolution is fundamentally limited by the channel size [7]. Vinelli et al managed to reach an average resolution of 60 µm (full width at half maximum) for a single particle while doing real-time positron beam monitoring – however, resolutions of under 10 µm have been reached by utilizing cross strip charge division readouts instead of phosphor screens when detecting photons [8].

An alternative – and generally more widespread – technique for real-time beam detection consist of partially blocking the beam and quantifying its interaction with the stopper. Commonly referred to as the knife-edge method, this approach does not directly return an image of the beam, but can at most detect its presence and intensity. While it is possible to infer the position and size of the beam through scans and a few basic assumptions, the information that can be gathered this way is limited and often insufficient to fully optimize the positron beam. Furthermore, scans aimed at determining the beam position and size are time consuming and often erode major portions of the available experiment time [5].

The novel approach to the problem of beam characterization being investigated in this thesis consists of directly imaging a positron beam using commercially available,

low-cost image sensors. The potential benefits such a system could offer include a higher resolution, faster acquisition and easier deployment compared to existing beam monitoring setups. Those improvements will ultimately aid in achieving smaller spot sizes and reduced focusing times.

The proposed mechanism for using said optical sensors with positrons is to coat them with a thin layer of phosphorescent material and expose them directly to the low-energy positron beam. The suggested type of phosphor is silver activated zinc-sulfide (ZnS:Ag), which has already been shown to exhibit positron-induced luminescence even at low implantation energies [9]. Its emission spectrum is centered around 450 nm, corresponding to deep blue visible light. The emitted photons can then be detected by the image sensor underneath, allowing us to directly image the shape of the impinging positron beam. It might even be possible to forego the use of phosphor and detect the positrons using the sensor itself. This hypothesis shall also be tested within the scope of the thesis and if confirmed might lead to further investigation of the specific mechanism involved.

One of the main challenges to overcome will be the relatively low particle flux of a positron beam. Compared to the amount of photons hitting a camera sensor under typical lighting conditions, the number of positions in a particle beam is spectacularly low. The primary beam of NEPOMUC for example - the single most intense positron beam in the world - reaches a particle flux of roughly 10^7 Positrons per second per square millimeter [10]. Assuming a unitary positron-to-photon conversion ratio within the phosphor, this corresponds to a light intensity of around 2.5 mLux - an amount roughly equivalent to a scene lit by starlight [11]. However, since the FRM 2 research reactor is currently offline for maintenance and repairs, the NEPOMUC beam will not be available during the time of my thesis. As an alternative, a much weaker positron beam located within the Heinz-Mayer Leibniz Laboratory (MLL) in Garching will be used to perform the measurements of this thesis. The positron flux achievable there will be another four orders of magnitude lower than the example just stated.

For those reasons it will be imperative to push the CMOS sensor to its absolute maximum sensitivity - way outside the range required for optical photography. Additionally, it is possible to increase the light emitted by the phosphor by increasing the energy of the positron beam. Stenson et al have showed that the positron induced luminescence of ZnS:Ag increases sharply with acceleration potential [9]. (Figure 1.1) A tenfold increase in luminosity was observed at an attractive bias of 5 kV.

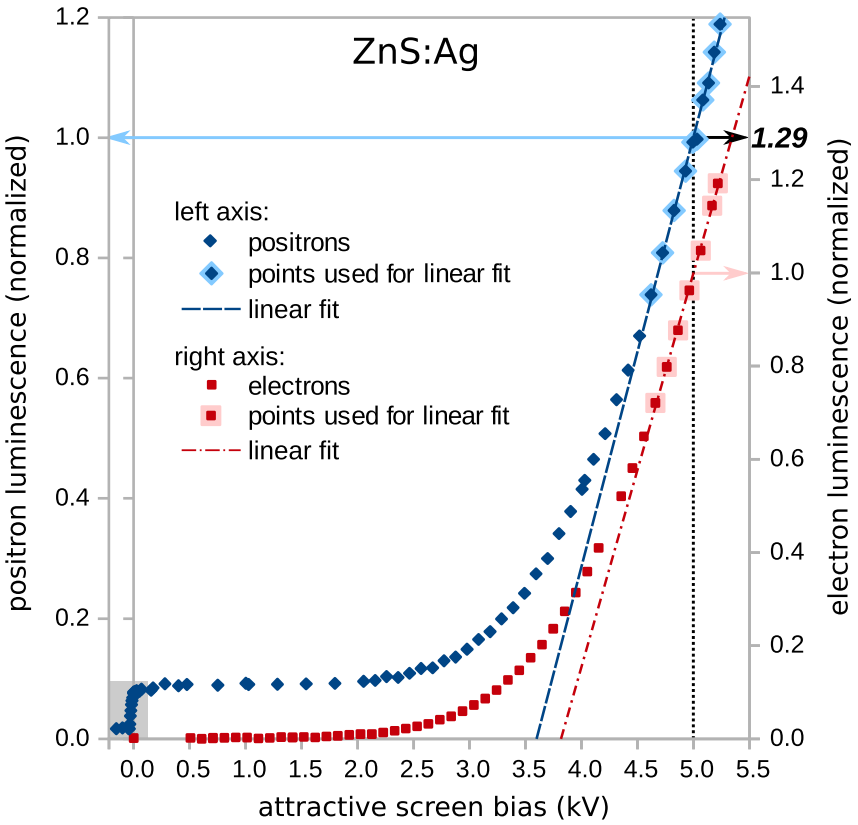

Figure 1.1: Dependence of ZnS:Ag luminescence on attractive screen bias for positrons (blue diamonds, left y axis) and electrons (red squares, right y axis). Image from [9]

2 Basics

The existence of antimatter has - somewhat famously - been mathematically predicted before being experimentally observed. In a pristine example of applied mathematics, the equations introduced in Paul Dirac's 1928 paper titled "The quantum theory of the electron", allowed for electrons to either have positive or negative energies as their solutions [12]. Driven by this irrefutable mathematical fact, Dirac published a follow up paper in 1931 in which he predicted the existence of a particle he called the "anti-electron". This yet-to-be-observed particle would have the same mass but the opposite charge of an electron and would annihilate itself and the electron upon contact [13]. Merely a year later in 1932, the anti-electron was observed by Carl David Anderson while he was studying cosmic rays passing through a cloud chamber. The particle was subsequently christened the positron and constituted the first evidence of antimatter.

2.1 Positron Physics

2.1.1 Properties of Positrons

Being its antiparticle, the positron shares many physical properties with the electron [14]. Their rest mass, rest energy and spin are equal but their charges are opposed. Being the positively charged antiparticle of the electron (denoted as e^-), the positron is symbolized with "e^+".

In vacuum the positron can be regarded as a stable particle. However, when implanted into a sample of ordinary matter, the chance of annihilation with electrons drastically decreases their lifetime. When a positron and an electron annihilate, their combined mass is released as energy - predominantly in the form of two γ-photons [15].

2.1.2 Positron Sources

Today, positrons can be artificially created via three main techniques. The simplest approach - often used in small laboratory setups - makes use of radioactive nuclides undergoing β^+ decay. Typical examples are the Isotopes ^{22}Na, ^{58}Co and ^{64}Cu. These sources are produced off-site and can simply be purchased as needed. However, due to their rather short half-lifes, they need to be periodically replaced as their activity decreases [5].

In setups where higher intensities are required, positron researches usually employ sources based on the principle of pair production. A high energy photon with at least twice the positron's rest energy is needed to create an electron-positron pair. This conversion can only happen by interacting with another particle - typically an atom with a high atomic number (Z). Suitable materials are therefore often referred to as high-Z converters and typically include Tungsten or Platinum [16]. One method of driving this conversion process features the use of high energy electrons produced by a particle accelerator. The electrons are dumped into a target of suitably high atomic mass which causes them to slow down and loose their energy in the form of bremsstrahlung. The so generated photons in turn interact with the high-Z material and are converted into electron-positron pairs [17].

Alternatively, a nuclear reactor can be used to generate the high energy photons needed. At the Delft University of Technology in the Netherlands, the γ-radiation produced by the fission reaction itself is used to drive pair production in an assembly of Tungsten foils [18]. A slightly different approach is implemented at the research neutron source Heinz-Maier Leibnitz (FRM II) in Garching, Germany. Here, a stream of thermal neutrons is used to drive the nuclear reaction of converting ^{113}Cd into ^{114}Cd, releasing γ-radiation in the process. These photons are then converted into electron-positron pairs in an adjacent Platinum structure [19]. Using this principle, NEPOMUC (NEutron induced POsitron source MUniCh) is able to generate a continuous beam of positrons with an intensity of $1.14 \cdot 10^9$ e^+/s, thus making it the strongest positron source in the world.

2.2 Positron Beams and their Applications

Most modern positron-based techniques require the production of a focused low-energy positron beam; which is achieved by firstly moderating the positrons and then by using magnetic and electric fields, to guide, accelerate and focus them into a beam shape. The

benefits that can be so accomplished include the ability to distance the sample being investigated from the source and hence reduce unwanted background radiation, being able to vary the positron energy by means of imposing an acceleration voltage and, most importantly, to localize the implantation by focusing the beam to a point.

2.2.1 Beam Guidance and Focusing

Being charged particles, positrons are influenced by electric and magnetic fields. They can be accelerated by electric and deflected by magnetic potentials. By carefully exploiting these forces, a variety of guiding and focusing elements can be constructed whose functionality often resembles that of components used in light optics [20].

One example for the use of fields in beam guidance is the transport of charged particles along the beamline. In the case of low energy particle beams this can be achieved by generating a uniform magnetic field pointing in the desired direction of travel. By choosing vacuum tubes made from non-magnetic materials, such a coaxial field can be generated by wrapping the beamline in isolated wires and passing direct current through them. A non-relativistic particle with charge q and velocity v interacting with a magnetic field B will experience a Lorentz force

$$\vec{F_L} = q\vec{v} \times \vec{B}.$$

By applying this equation to a positron traveling through the coaxial magnetic field, any transverse velocity component of the particle will induce a gyration motion centered around the field lines. Any longitudinal velocity component will not induce a Lorentz force since it constitutes a motion parallel to the field lines. The resulting path of the particle will therefore describe a spiral along the applied field lines. The radius of this spiraling motion r_g can be calculated by equating Lorentz force and centrifugal force

$$F_z = \frac{mv^2}{r}$$

$$qv_\perp B = \frac{mv_\perp^2}{r_g}$$

$$r_g = \frac{mv_\perp}{qB}$$

where m is the particle's mass and $v_\perp$ its transverse velocity [5].

Even for a relatively simple setup, many more coils and electric potentials are required to produce a well collimated and focused positron beam. Further examples include Helmholtz fields, correction fields and focusing lenses. And although crucial for the experimental part of this thesis - these techniques shall not be further described here. It should however be noted, that the task of guiding and focusing a positron beam requires iterative adjustment of many dependent variables (i.e. coil currents and acceleration voltages).

2.2.2 Beam Monitoring

Information about the shape and intensity of a positron beam is an essential requirement to the effective operation of a low-energy positron beam. A variety of methods, some of them applicable to particle beams in general, have been developed to measure the position, shape and intensity of a positron beam.

Micro Channel Plates (MCPs)

A frequently employed setup utilizes micro-channel plates (MCPs) in combination with a phosphor screen and a scientific camera to measure beam shape and sometimes intensity in real time. An MCP detector consists of one or more stacked plates perforated by an array of microscopic channels, usually slightly tilted with respect to the longitudinal axis of the plates. While the channel diameter is on the order of microns, the plates themselves can be tens of millimeters in size, resulting in an area of detection of several square cm. A voltage difference in the kilovolt range is applied between the front and back of the plate, making each channel act as an electron multiplier. A particle, be it an electron, positron, ion or high-energy photon striking the inside of a channel will produce a shower of electrons via secondary emission. The signal produced by a particle entering a channel can thereby be amplified by a factor of up to 10^7. The resulting intensified electron emission is then further accelerated by an electric potential before impinging on a phosphor screen placed some distance beyond the plate. The phosphor screen converts the electron signal into visible photons which can then be detected by a camera, usually placed outside of the vacuum system [6, 7].

MCP detectors can be manufactured and adjusted to accommodate a wide range of setups. Using advanced readout electronics they can reach sampling rates in the GHz or be used as single particle detectors [21]. They are however limited in their spatial

resolution, mainly by the geometry of the channels (i.e. their diameter and spacing) and the phosphor grain size [7]. Vinelli et al managed to reach an average resolution of 60 µm (full width at half maximum) for a single particle while doing real-time positron beam monitoring. Resolutions of under 10 µm have been reached by utilizing cross strip charge division readouts instead of phosphor screens when detecting photons [8].

Knife-Edge Method

When working with very small or precise beam shapes where MCPs cannot provide the necessary resolution, positron researchers usually resort to the so-called knife edge method. This relatively simple, yet effective technique is traditionally used in light optics to measure laser beams but can be nicely adapted to positron beams as well [5]. When used with lasers, the setup consists of a very sharp edge - often a razor blade - mounted on a linear actuator. The actuator moves the edge very precisely into the laser beam, partly blocking it. A monitoring system then measures the remaining beam intensity quantifying the amount of attenuation caused by the knife edge. By correlating the exact position of the edge with the measured attenuation, it is possible to deduce the beam profile along the axis the knife edge was moved in. The technique is often performed twice, along perpendicular axes so that an elliptic approximation of the beam cross section can be generated. The spatial resolution of this type of measurement is mainly limited by the resolution with which the edge can be positioned [22]. Araujo et al have used this method in combination with an updated mathematical model to characterize their laser beam to within $\pm 60\,\mathrm{nm}$ [23].

In order to adapt this method for positron beams, the literal knife edge has to be replaced by a solid sample featuring a sharp transition between two materials. The materials chosen should exhibit distinctly different interactions with positrons in order to be easily differentiated by whatever detection system used. One possibility - as demonstrated by Gigl - is to use Doppler broadening spectroscopy (DBS) to distinguish between strips of copper foil and the aluminum base material they are mounted on [5]. The use of DBS in this application was particularly practical since the beam was being characterized for the ultimate use in a coincident Doppler broadening spectrometer. Other setups can take advantage of the variation in intensity when positrons are back scattered by different materials. A sample consisting of a Tantalum ribbon mounted onto a base of SiO_2 can be used as a knife edge when measuring back scattered positron intensity [24].

One distinct drawback of the knife edge method however is its acquisition speed. Since the carriage has to be physically moved across the beam and some sort of measurement performed at every increment, capturing a complete beam profile takes a significant amount of time. The time required to measure the beam width depends mainly on the resolution requirements and the method to detect the edge transition, but typically ranges between 15 minutes and more than an hour. Furthermore, even when using two perpendicular axes to scan along - as is usually the case - it is only possible to measure the projection of the beam across the measurement axes. When reconstructing a beam shape from these projections it is necessary to make additional assumptions - typically an elliptical cross section of the beam is assumed. This is the case because any asymmetry of the beam across the scan axis will be averaged out. Therefore, when using two scan axes, the most complex shape that can be uniquely assigned is an ellipse.

3 Modern Image Sensors

The great advances made in semiconductor manufacturing over the last decades have enabled the mass production of miniaturized and highly capable image sensors. The ability to capture images with millions of pixels and high frame rate videos are now standard features of modern smartphones. This chapter aims to give a brief overview of the imaging technologies making this possible.

3.1 Charged Coupled Devices (CCDs)

Digital imaging sensors are typically implemented using one of two fundamentally different technologies: Charged Coupled Devices (CCDs) and Complementary metal-oxide-semiconductor (CMOS) sensors. Both types of sensors exploit the photon-induced electron excitation to generate a free electric charge from incident light. Photons with an energy large enough to overcome the band gap of Silicon (approx. 1.12 eV at 300 K) will create electron-hole pairs as they enter the sensor material.

In a CCD an electric field is used to draw the so created conduction-band electrons into an area of conductive Silicon called the channel. While the sensor is collecting light, the photo-electrons are confined to a specific region within that channel by an array of electrodes. Those electrodes are separated from the channel by a layer of insulating material to form a metal-oxide-substrate (MOS) structure. In Figure 3.1 the cross section of such a sensor is shown. In this example, each pixel is made up of three electrodes. By applying a positive voltage to the middle electrode while keeping the other two at ground potential, the photo-electrons can be spatially confined in the channel [25].

After collecting charges for a given exposure time, the electrons stored in each pixel are shifted to the next by sequentially applying positive and negative voltages to the electrode array. This happens simultaneously at every pixel along a given row. At the very end of each row the charges are shifted into a special column of capacitors that will transport the charges towards a centralized amplifier in the same manner. There the

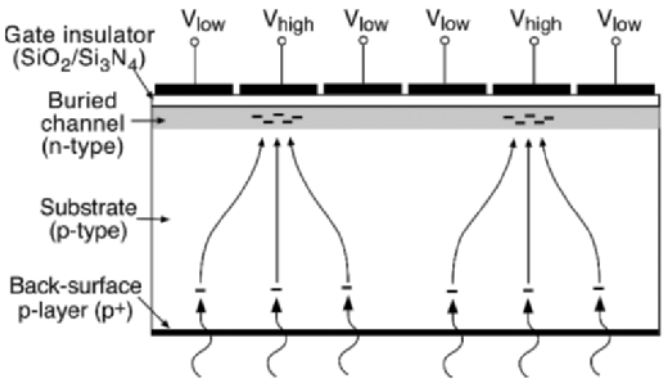

Figure 3.1: Cross sectional view of a CCD. The photons coming from below generate charges in the Silicon which are subsequently collected and confined in a conductive channel. Image from [25]

packets of electrons are amplified into an analogue signal which can then be digitized. (Figure 3.2)

This approach offers the advantage of having a very uniform pixel response even across large sensors since each pixel is relatively simple in construction and read out by the same output amplifier. Additionally, this amplifier can be optimized for low noise and high performance without restrictions on physical size since it can be located elsewhere on the Silicon dye. These properties, combined with the fact that the charge shifting is extremely efficient in terms of preserving the collected charges, yield a very high signal-to-noise ration for CCDs. Similarly, dark current and fixed-pattern noise are very low, making CCDs well suited for scientific applications.

For all their advantages in operation however, their fabrication requires special materials and processes. High volume production lines set up for logic and memory devices usually cannot facilitate the production of CCDs, which ultimately drives up their cost. Furthermore, since the pixels can only be read out sequentially, CCDs are limited in their acquisition speed - both by the amplifier bandwidth and the charge shifting [25].

3.2 CMOS Sensors

To avoid the shortcomings of a CCD, CMOS image sensors take advantage of the same highly integrated circuit technology that is used in microprocessors and memory devices. While the very first stage of converting light into a signal via the photoelectric effect is identical in both types of sensor, the amplification stage of a CMOS sensor is directly

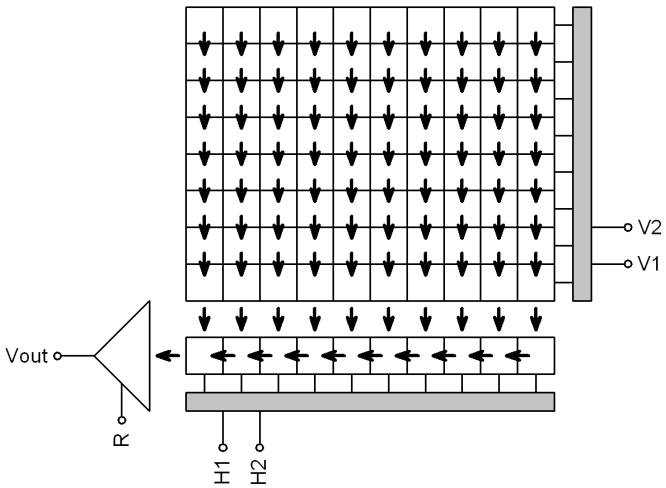

Figure 3.2: Schematic of reading out a CCD. The charge packets generated in each pixel are shifted - first along their row and then along a dedicated column - towards the readout electronics. Image from [26]

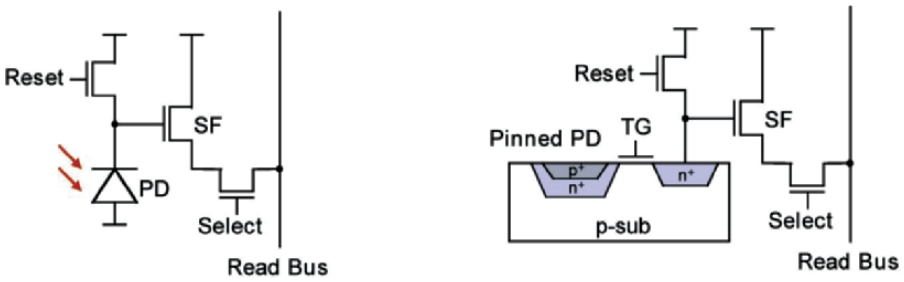

Figure 3.3: On the left, a minimal design for a CMOS-type imaging sensor pixel, requiring only three transistors per pixel on the active area. On the right, a fourth transistor has been added which allows the control of the exposure time. Image from [27]

integrated into each pixel. These active pixels are then multiplexed during readout using integrated CMOS switches to generate the image. The digitization of the amplified signal is then handled by an analogue to digital converter (ADC) placed elsewhere on the dye [27].

CMOS sensors offer a very high level of flexibility in pixel design, on-chip processing and even photodiode material. In the very simplest case, three transistors per pixel are necessary to achieve amplification and multiplexing capabilities (Figure 3.3). However, more complicated pixel designs with hundreds of transistors exist, offering per pixel ADC conversion and other special features.

Because each pixel features active components, they will exhibit slightly different properties and amplification factors. These differences have to be characterized and taken into account, usually by calibrating each sensor during manufacturing and storing the results

on-chip. The sensor can then automatically compensate for nonuniformities between pixels. Another distinct drawback of CMOS image sensors is their so-called fill factor. A CCD can be so designed as to utilize the entire area of a pixel to collect photons - its fill factor is 100%. In a CMOS sensor however, since each pixel has to accommodate at least three transistors, only part of the pixel can be made photosensitive. Since the effective quantum efficiency - the ratio between charge carriers collected and photons hitting the pixel - is dependent on the fill factor, CMOS sensors are limited by their construction in this regard [27].

To compensate for their limited fill factor, modern CMOS sensors can make use of one or both of the following techniques. Firstly, using advanced manufacturing processes it is possible to place the active components of a CMOS pixel behind the photosensitive layer, thus reducing the amount of light being blocked and directly increasing the fill factor. This type of arrangement is referred to as back-side illumination. A schematic comparison to the more traditional front-side illumination is shown in Figure 3.4. However, even in back-illuminated sensors a small dead zone between individual pixels is necessary to electrically isolate them. To overcome these losses, manufacturers usually place a microscopic lens on top of each pixel in order to focus incident light onto the sensitive area of the pixel below. Such microlens arrays can be employed in both front and back-illuminated sensors and also help to reduce optical crosstalk between pixels [28].

Except when specifically designed to be used in scientific or industrial settings, commercial images sensors are usually manufactured to produce color images. However, since any photon with high enough energy will create charges in the photosensitive layer, both CCDs and CMOS sensors themselves do not discriminate between different wavelengths of light - i.e. they are monochrome sensors. In order to distinguish the colors of incoming light, a pattern of subtracting color filters is placed on top of the pixel array. The most commonly used arrangement of colors is known as the Bayer pattern. This type of filter covers half of all pixels in green, one quarter in blue and one quarter in red - alternating over the entire sensor. Figure 3.5 shows the arrangement of the Bayer filter on top of an array of pixels. By so filtering the light each pixel receives, a post-processing algorithm can later infer an RGB color value for each point in the image by averaging the values of the correspondingly colored adjacent pixels. This step is referred to as demosaicing and a variety of different algorithms exist [29].

Even though CMOS image sensors are worse off in pixel uniformity and noise characteristics when compared to CCDs, their greater flexibility and higher acquisition speed

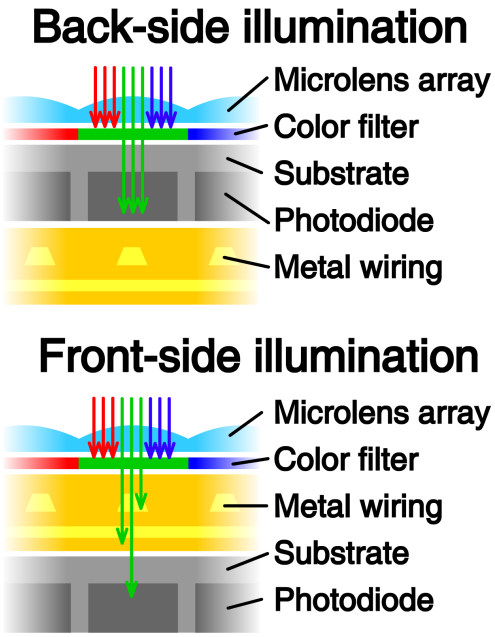

Figure 3.4: Back-side vs front-side illumination in CMOS sensors. Both examples also feature a microlens array and a color filter

make them the obvious choice for consumer devices. Additionally, the highly optimised CMOS technology used make them significantly more energy efficient compared to a CCD. Due to those advantages, the consumer camera sector almost exclusively uses CMOS sensor technology. Today, CCDs are more commonly found in specialized cameras for scientific or medical applications where demands for image quality are higher. In Table 3.1 a summarized comparison between the two sensors types is given, listing their respective advantages and drawbacks [25].

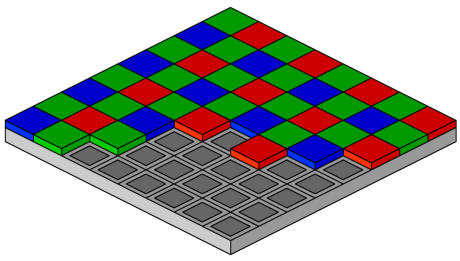

Figure 3.5: The alternately colored Bayer filter on top of an array of monochrome pixels.

CCD Sensors	CMOS Sensors
Highly optimized for optical detection, special fabrication requirements	Benefits from advances in manufacture of high-volume digital products
Very high signal-to-noise	Noise typically higher
Low photoresponse nonuniformity (PRNU), low fixed-pattern noise (FPN)	High PRNU, high FPN, improved by gain and offset correction
Low dark current	Dark current typically higher
High power dissipation	Low power consumption
Complex driver electronics, no on-chip logic and digitization	Usually single power supply operation, digital output
Serial readout, limited windowing capability	Random addressing capability

Table 3.1: Summary Comparison of CCD and CMOS Technologies. Table from [25]

4 Sensor Selection and Characterization

In order to gauge the feasibility of using ordinary image sensors as positron detectors, three different CMOS sensors were selected and extensively characterized. Since the sensors would be operated way outside of their intended limits, the information contained in the datasheets provided by the manufacturer is of limited use. Therefore, a range of different tests was conducted in order to explore their behaviour in those extreme use cases. No CCD sensors were considered for the experiments of this thesis since the greater flexibility and lower cost of CMOS devices make them more suitable for the proposed use case.

4.1 Selection Criteria and Limitations

As a starting point for experimentation, a few inexpensive USB-webcams were purchased and their image sensors inspected. A camera by the designation of RF-WC1080P1 was chosen for first experiments - mainly for its large sensor area and ease of disassembly. It is built around the Omnivision OV2735 - a low cost, general purpose CMOS image sensor. The aim of these preliminary tests was to assess the low-light sensitivity limits of the sensor and on-chip image processing.

After promising initial results, two more CMOS sensors where purchased - the IMX219 and the IMX477, both produced by Sony. These sensors are most commonly known for their use in the Raspberry Pi's "V2" and "High Quality" camera modules. The camera modules are breakout boards designed around the aforementioned chips, providing the bare minimum hardware required to interface with the sensors. They allow for low level hardware control and are marketed towards hobbyist - thus a wide range of open-source projects and even some scientific literature exists around them.

4.2 Communication Protocols and Readout Electronics

In order to process the data with the rigor required by a scientific investigation of the sensor's capabilities, it is desirable to receive the captured images in their raw, uncompressed state. Most camera systems are not setup to stream raw images in this fashion as the bandwidth/storage requirements are not easily accommodated and the advantages are typically slim. We were able to record raw images from all of the sensors we characterized but, as we will shortly see, not without having some measure of compromise.

4.2.1 Omnivision OV2735 (RF-WC1080P1)

After disassembly and reverse-engineering of the RF-WC1080P1's circuitry, the block diagram shown in Figure 4.1 was drawn up – depicting the basic signal flow through the device. At its heart sits the SPCA2281B3 web cam controller – an integrated circuit designed to handle all mayor aspects of a USB webcam. It communicates with the OV2735 image sensor via standard I^2C protocol and receives pixel data using the MIPI Camera Serial Interface 2 (CSI-2). This type of interface features one differential clock and up to four differential data lanes and is the most widely implemented embedded camera interface to date. It can support extremely high data rates which allows the image sensor to transfer the pixel data uncompressed and in real time to the webcam controller IC. In this case, the OV2735 specifies a maximum image transfer rate of 30 frames per second at the full resolution of 1080×1920 pixels. The sensor features a 10-bit ADC, resulting in a required transfer speed of at least

$$1920 \cdot 1080 \cdot 30 \cdot 10 \simeq 622 Mbps$$

The CSI-2 V2.0 used by this sensor can accommodate a theoretical transfer rate of 4.5 Gbps per data lane - of which the OV2735 uses two.

The webcam controller IC then processes the incoming pixel data by demosaicing and compressing the acquired frames. Some sort of compression is necessary, because the recorded images are subsequently transferred to the host device via the USB 2.0 Hi-Speed protocol, the maximum theoretical transfer rate of which is 480 Mbps - too little to transfer the images at full frame rate without compression. To accomplish this, the SPCA2281B3 IC applies the Motion JPEG (MJPEG) compression format - a technique by which each frame of an image stream is separately compressed as a JPEG image.

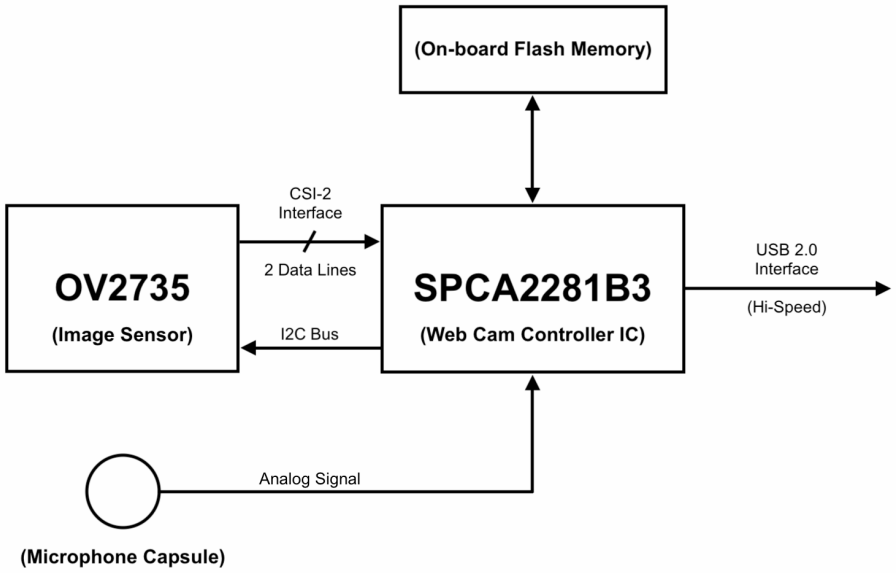

Figure 4.1: Schematic depicting the basic signal flow of the RF-WC1080P1 webcam.

While great for reducing the bandwidth requirements, this approach comes with certain caveats. The JPEG compression algorithm works best on images that display a smooth variation of tone and color, which is true of most natural scenes - hence its great effectiveness when working with photographs. Issues arise however when one compresses an array of pixels that features sharp contrasts in close proximity. In a nutshell, the algorithm degrades the high-frequency component of the image signal and, as a result, large differences between adjacent pixels will tend to get averaged out and potentially useful data might get lost. Hence, this mode of operation was unsuitable for the purposes of this thesis.

As an alternative, the webcam controller can be configured via USB to provide uncompressed frames in the YUV color space - albeit at a reduced frame rate. The specific format used is known as the YUYV422 pixel format and it further reduces the bandwidth requirements by sub sampling the pixel's color information - in this context known as the chrominance values. Since the human eye is more sensitive to luminance (metric of perceived pixel brightness) than chrominance, the loss of color samples does not have a significant impact on image quality. For the planned experiments of this thesis, color information is not relevant at all, making this pixel format a suitable choice.

A major drawback of the RF-WC1080P1 camera was however, that it was not possible to receive the images without having the demosaicing algorithm applied to them. Since the Bayer filter would later be removed from the sensor in order to maximize its sensitivity,

applying the demosaicing step skews the pixel data and causes unnecessary distortions in pixel luminance.

To interface with the camera via USB, the Video4Linux2 (V4L2) drivers were used. V4L2 is a collection of Linux drivers made for capturing live video from a variety of devices. Using the accompanying v4l2-ctl command line application, different camera settings like brightness, gain, exposure time or pixel format can be set - and a specified number of frames subsequently acquired. Although the V4L2 drivers allow for very fine control over the camera's settings in this manner, a more low level approach would have been preferred. Unfortunately, our attempts to contact SunplusIT - the manufacturer of the SPCA2281B3 controller - to recover the controller's datasheet were met with no reply.

4.2.2 Sony IMX Series

In contrast to the RF-WC1080P1 webcam, the Raspberry Pi camera boards around the IMX219 and 477 feature only passive components and cannot be interfaced with via USB. Instead, the sensor directly communicates via the CSI-2 with a suitable host device using a 15 pin flex cable. In this case the host device has to feature the correct version of the CSI as well as provide the necessary processing power to demosaic and compress the frames. The most commonly used - and by the manufacturer intended - host devices for this purpose are the infamous Raspberry Pi single board computers (SBCs). They come equipped with the necessary 15 pin ZIF connector by default and the software can be easily configured to work with the camera modules. Although many different camera controllers and processors could be used with these sensors, for the purposes this thesis the Raspberry Pi 3B+ SBC was chosen for its ease of use and abundance of documentation regarding the camera interface. However, at the time these experiments where conducted, nearly all models of the Raspberry Pi SBC where unavailable due to the global microchip shortage. Therefore, the two 3B+ SBCs used in this thesis had to be salvaged from previous personal projects.

The program chosen to control and read the sensors via the Raspberry Pi's CSI is a command line tool called raspiraw. This application is based on a software stack using proprietary Broadcom GPU code, which is why Raspberry Pi is in the process of transitioning to a different, open-source implementation and considers raspiraw part of its legacy stack. None the less, the libcamera project that is currently aiming to replace this legacy stack has been found to lack certain features for low level communication

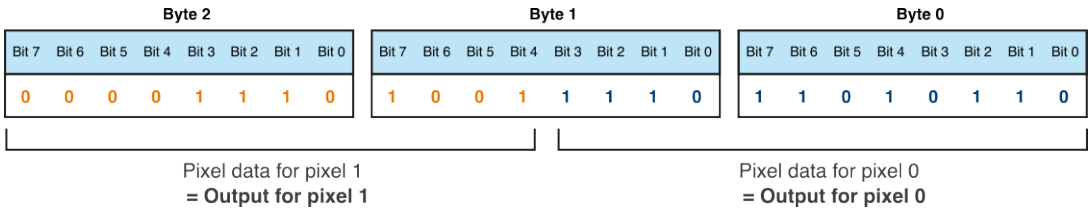

Figure 4.2: Packing order in the case of 12 bit pixel data. Each pixel value spans one and a half bytes, reducing the bandwidth requirements but requiring additional processing power to unpack on the target device. Image from `https://docs.baslerweb.com`

that are essential in unlocking the image sensors full potential. The choice has therefore been made in favour of the raspiraw camera software.

The IMX series image sensors can be configured via an I^2C bus by setting a range of internal sensor registers to the desired values. The datasheet of the IMX219 is publicly available and provides detailed information on the available registers and their function. The raspiraw tool offers a variety of predefined camera modes that translate into a set of camera register values which are optimized for different resolutions or frame rates. Alternatively, the user can specify their own register inputs, allowing for hardware level control over the sensor.

On top of the great level of fine control, this setup also delivers the acquired frames in their most raw, packed state - without compression or demosaicing. In order to generate a viewable image in the first place, the byte stream that is received from the sensor has to be unpacked. This process is necessary, because the IMX219 and 477 feature a bit depth of 10 and 12 bits respectively while data is handled by the CPU in octets. Data is transferred from the sensor with each pixel data spanning more than a single octet (Figure 4.2) No bandwidth is wasted this way but additional processing power is necessary in order to unpack the pixel data into a useful format. To this end, a simple program was written in C++ that handles this unpacking process for both types of sensor.

While the complete datasheet of the IMX219 sensor is freely available on the internet and provides all of the necessary information for correctly setting the sensor's registers, documentation on the IMX477 sensor is more sparse. Only a partial datasheet is available which, crucially, lacks information about the sensor's registers. In an attempt to recover the necessary information, the relevant subdivision of Sony has be contacted - without success. Therefore the functionality of this sensor had to be explored by reverse engineering parts of the raspiraw software and gathering pieces of information online.

While this process yielded acceptable results in terms of sensor control, it is likely that we were unable to reach the chip's full potential in these tests.

4.3 Experimental Setup for Sensor Characterization

In order to characterize the performance of image sensors in extremely low light conditions, a setup was devised in which the sensor of interest can be exposed to a well known quantity of light. The system consists of a completely light tight box wherein the camera sensor is illuminated by an LED. The distance from the diode to the sensor is known and the inside surfaces of the box are designed to minimize reflections and light diffusion so as to only allow light coming directly from the LED to hit the sensor. By driving the LED with a carefully controlled current, the amount of light the sensor is exposed to can be precisely set. Since the emission spectrum of the proposed phosphor is known and within the visible spectrum, an LED with a wavelength similar to that of the phosphor was chosen. That way the LED closely emulates the light emitted by the phosphor. Apart from gauging the limits of sensitivity, this setup can also be used to determine other characteristics of the sensor relevant to the measurement like linearity, dark count or the temperature dependence of any of its characteristics.

4.3.1 Chamber Design and Geometry

Main objectives for the test chamber's design were to provide a firm mount for the different camera boards, minimize surface reflections and light diffusion, and provide a way of consistently varying the distance from LED to sensor. A cross section of the chambers final layout is shown in Figure 4.3. The setup consists of a main chamber that has the sensor mounted on the inside and facilitates a number of movable inserts. These inserts are designed in such a way as to direct any light that might be reflected or scattered by their surface away from the sensor. (see Figure 4.4). The movable inserts all have a fixed thickness of 10 mm and can be stacked on top of each other, allowing the distance from LED to sensor to be varied by adding or removing inserts. At the very back of this stack a similarly shaped insert is placed that houses the LED at its center. The assembly is then held in place by a compression spring which takes up the remaining space.

The cables connecting both the image sensor and the LED were routed along a convoluted path to an opening at the back of the chamber where they exited the setup.

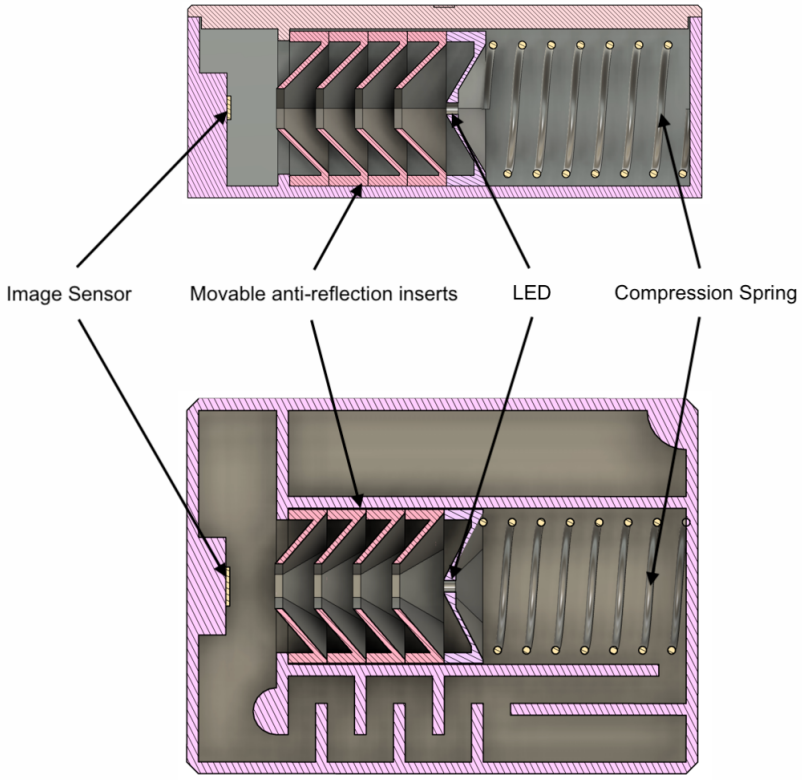

Figure 4.3: A horizontal and vertical cross section of the LED test chamber with its major components labeled. The assembly was printed from matt-black PLA plastic using a 3D printer.

Afterwards, the area around the opening was stuffed with black packaging foam. These measures were aimed at reducing light leakage entering through the path of the outgoing cabling. The lid - which was similarly designed to minimize light leakage - could then be mounted onto the box via two screws. The entire setup was printed from matt-black PLA plastic using an FDM 3D printer.

4.3.2 Geometry of Light Output

In order to precisely calculate the amount of light the sensor receives in this setup, it is necessary to take the angular distribution of the LED's light output into account. This property - often called the radiation characteristic - states how much light the diode emits in any given direction. It is mainly influenced by the LED's built-in lens, which is designed by the manufacturer to produce a desired output profile.

For the experiments of this thesis, an LED by the designation of LB Q39G has been chosen for its output wavelength which most closely matches that of the proposed

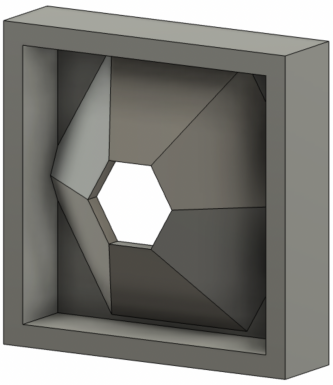

Figure 4.4: CAD model of one of the movable inserts designed to reduce light reflection into the sensor. They were similarly 3D printed from PLA plastic.

phosphor. A plot of the relevant radiation characteristic is shown in Figure 4.5. Since this LED is manufactured in a rectangular SMD package, the datasheet provides us with two curves - one for each plane of symmetry. Each point on those curves describes how much light per solid angle is emitted in a given direction in that specific symmetry plane.

To calculate the light output which the sensor will receive, the two curves where first digitized by manually marking several points on the plot and interpolating them polynomially. In order to simplify the calculations, the two curves were then averaged to get a function that is valid for every angle - put differently, the light output of the LED was assumed to be, in first approximation, radially symmetric. Then, the angle that the image sensor covers is calculated via simple trigonometry. Finally, the fraction of the total light output that is received by the sensor can be determined by integrating the LED's radiation characteristic - of which we have just formulated an interpolation - over the image sensor surface. At a typical distance of 50 mm, it is found that around 1 ‰ of the LED's light output is received by the sensor.

4.3.3 LEDs at Very Low Currents

In order to quantify the light flux that the sensor will receive, the conversion efficiency of the LED has to be taken into account. Ideally, each electron that transverses the LED causes the emission of a photon. In this case, the total light flux of the diode could be calculated by dividing the current flowing through it by the elementary charge e - resulting in the number of electrons per second flowing through the device. In a 100% efficient LED, this equals the number of photons generated.

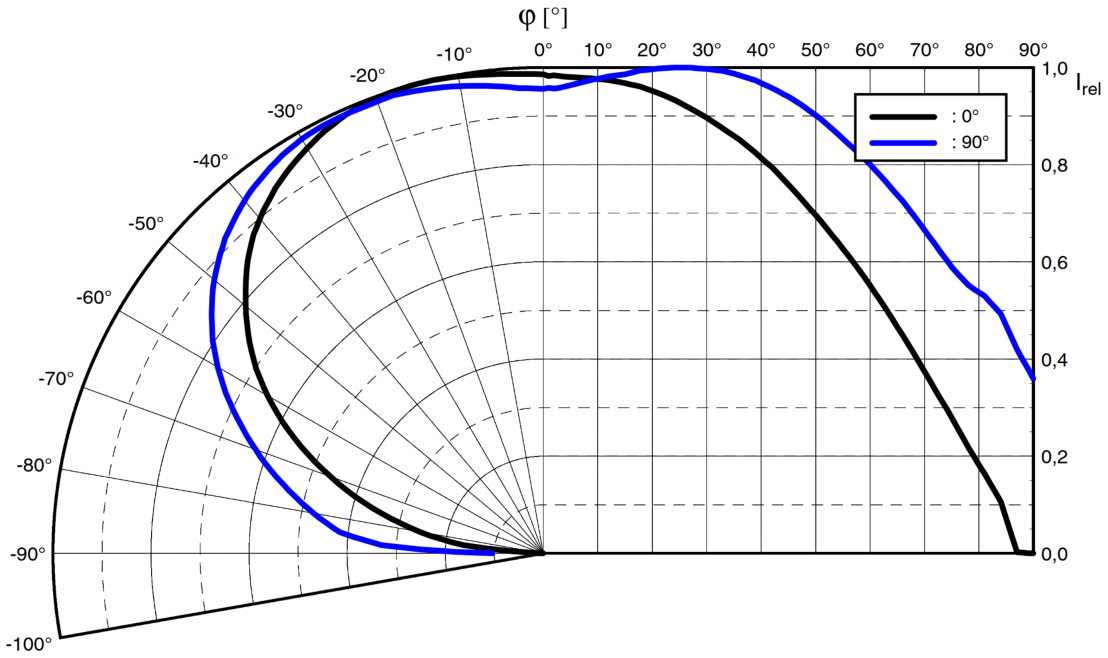

Figure 4.5: The radiation characteristic of the LB Q39G. The two curves each represent the light distribution over one plane of symmetry. Image from [30]

In reality, different effects in the semiconductor junction can reduce the LED's efficiency significantly. Most notably, LEDs exhibit a substantial drop in efficiency when used in high power applications where the current densities inside the device are relatively high [31]. At comparatively low currents however, blue Indium-Gallium-Nitride (InGaN) LED's - such as they are used in this setup - have been shown to achieve wall-plug efficiencies of 78% to 83% [32, 33]. The wall-plug efficiency (WPE) in this context is defined as the ratio of light output power to electrical input power and puts an upper limit on the diode efficiency. For the experiments of this thesis the LB Q39G LED has been calibrated using a Thorlabs FDS100 photodiode and measured to posses a WPE of around 34%.

Due to its definition, the WPE also takes electrical losses inside of the LED into account - for example the voltage drop caused by internal resistance. While this is generally relevant when considering their overall energy efficiency, in these experiments only the ratio of emitted photons to injected charge carriers is of interest. The applied voltage potential that was necessary to transport the charges through the LED is irrelevant here. To distinguish the two, this ratio of emitted photons to pumped charge carriers shall be designated the electron conversion efficiency (ECE). The contributions of electrical losses to the WPE can be estimated by considering the diodes nominal forward voltage drop and the energy of the emitted photons. The datasheet of the LB Q39G states a

typical forward voltage of 2.85 V at a current of 5 mA and specifies the LED's dominant wavelength to be 470 nm. The energy carried by a photon can be calculated using

$$E = \frac{hc}{\lambda}$$

where E is the photon's energy in electron volts, h the Planck constant, c the speed of light and λ the photon's wavelength. For a wavelength of 470 nm this yields a photon energy of ≈ 2.64 eV. One can therefore estimate that $\frac{2.64}{2.85} \simeq 92.6\%$ of the input electrical energy reaches the semiconductor junction. Since these losses do not affect the electron-photon conversion, the ECE can be calculated to be around $\frac{34\%}{92.6\%} \simeq 37\%$. A typical LED current used for sensor characterization was 100 µA which would in this case yield a total photon flux of

$$\frac{0.0001}{e} \cdot 37\% \simeq 2.3 \cdot 10^{14} \text{ photons/s}$$

4.3.4 Driver Circuitry

In order to precisely set the LED's light output, a constant current driver circuit based on an operational amplifier (opamp) was designed. The system can be controlled via USB and allows the LED to be fed by a very low, carefully controlled current. A simplified schematic of the circuit is shown in Figure 4.6. A microcontroller (not shown) generates a pulse-width modulated (PWM) output which is fed into a second stage low-pass RC filter. The purpose of this filter is to smooth the PWM signal into an analogue voltage that can be fed into the TL082 opamp. In order to allow for a high output resolution, the PWM frequency used is very low at only 122 Hz. The filter therefore was designed to have a very low cutoff frequency of 0.34 Hertz and consequently exhibits a relatively long response time of up to 3s until it reaches equilibrium. The analogue output voltage of the filter stage has been measured to feature a maximum AC component of 10^{-5} V (peak-to-peak) which is in excellent agreement with the expected theoretical value.

The stable and finely controllable voltage generated by the filter stage is subsequently fed into the non-inverting input of the opamp. The output of the TL082 directly feeds into the LED which is connected to ground via a resistor. This resistor acts as a current shunt and will exhibit a voltage drop across it that is directly proportional to the current flowing through it and the LED. The so generated voltage relative to ground is then fed into the inverting input of the opamp, thus completing the feedback loop. The operational amplifier will always try to drive its output such that the voltage difference between its inputs goes to zero. During normal operation, the microcontroller provides

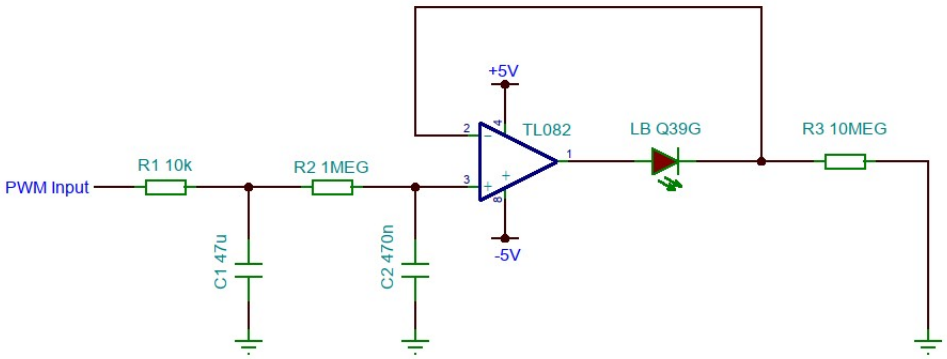

Figure 4.6: The schematic of the constant current driver used to power the LED to a set given current. The PWM modulated input signal is generated by a microcontroller (not shown).

a variable input voltage to which the opamp responds by sourcing just enough current through the LED so that the accompanying voltage drop across the shunt resistor equals the set input. Since the relationship between voltage drop and current is governed by Ohm's Law, the desired LED current can be easily translated into a voltage to be set by the microcrontoller.

4.4 Results and Parameter Optimization

4.4.1 Omnivision OV2735 (RF-WC1080P1)

Sensor Construction and Glass Cover

To protect the pixel array of an image sensor from debris and mechanical strain, they are usually covered by a thin layer of glass. Depending on the camera's construction, this glass cover is mounted either directly onto the Silicon die, the surrounding circuit board or the lens assembly. In the case of the OV2735 sensor, a 400 µm thick piece of glass is glued onto the sensor's substrate. The epoxy is dispensed along the edges of the glass, leaving a 45 µm air gap between the sensor surface and the glass.

Although this thin layer of glass has a negligible effect on the optical performance of the camera, it makes the sensor entirely unsuitable for detecting positrons. If one were to coat the top surface of the glass with phosphor and expose it to the positron beam, the light emitted by the screen would bleed into adjacent pixels and drastically reduce the spacial

resolution. Using the setup without phosphor - by directly implanting the positrons into the stack - would similarly fail, since the low energy positrons cannot penetrate far enough into the glass to reach the sensor's surface. It was therefore essential to develop a method of removing the glass cover from the image sensor. Using external force to separate the cover was not feasible, since the Silicon substrate features a thickness of only 100 µm and has mechanical properties similar to that of the glass.

Ideally, a chemical procedure would be used in which the epoxy gluing the cover glass to the sensor would be dissolved while leaving the substrate unharmed. Based on current manufacturing practices it is reasonable to assume that the epoxy used is a type of heat- or UV-curable adhesive that polymerizes to form a strong bond between the glass and Silicon substrate. The first approach was therefore to try a range of solvents that are commonly used to dissolve polymers. To that end, the chemicals listed in Table 4.1 have been tested - both at room temperature and at 70 °C by submerging the sensor-glass stack for several hours.

Tested Solvents
Ethanol
Acetone
Isopropanol
Toluene
Methanol
Acetic Acid
Undecane
Cyclohexane
DMSO
Dichloromethane
Trichloromethane
MELLERUD Glue Remover
MELLERUD Silicone Remover
RENOVO Paint Stripper
RENOVO Paint Stripper + Acetone
Sodium Hypochlorite
1M Sodium Hydroxide
30% Ammonium Hydroxide
40% Hydrochloric Acid
90% Sulfuric Acid
Fuming Nitric Acid

Table 4.1: The list of solvents tested for dissolving the glue bonding the cover glass to the sensor. The only chemical that yielded any results was Fuming Nitric Acid.

Frustratingly, the only chemical which was successfully able to separate the glass was fuming nitric acid at 70 °C. However, submerging the entire sensor in acid did also dissolve the solder pads and copper traces on the back of the device, rendering this method useless. Since the top surface of the sensor should be unaffected by the solution due to a Silicon passivation layer, a procedure in which drops of acid would carefully be placed on the side of the stack and drawn into the gap by surface tension was developed and tested. Since the acid would not come into contact with the sensor's underside, this method would leave the device intact and functional. Although first results showed partial success, this approach was ultimately abandoned for its high degree of manual labor and necessary safety precautions involved. The possibility of directly dissolving the glass using hydrofluoric acid or molten sodium hydroxide was briefly considered but quickly dismissed, as the chemical composition of the Silicon substrate very closely matches that of glass and would subsequently also be dissolved.

Since the need for removing an images sensor's glass cover is not unique to this project, different commercial options do exist. The company EURECA Messtechnik GmbH for example offers a glass removal service for a range of standard CCD and CMOS image sensors aimed at enabling UV or X-ray detection. Although the OV2735 is not listed in their repertoire of successfully converted sensors, the company was contacted for their expertise and advice in this matter. Regrettably however, they were not able to offer their services in this case since no technique of theirs would be able to work on this type of sensor package. Two more companies offering similar services - Pacificxray and Salvo Imaging - were contacted in this matter but were likewise unable to help.

As the cover glass would not drastically influence the sensor calibration using the LED, the tests where continued with the sensor unmodified. However, for the reasons stated above, the inability to remove the glass cover practically rendered this sensor unusable for positron detection.

Flat Fielding

While characterizing the OV2735 using the LED test setup, the appearance of multiple concentric circles in the center of the image was observed. The number and brightness of these circles varied with camera settings but usually appeared at very high gains and only when the sensor was illuminated. Noticeably, the circles in the center of the image always appeared darker than those towards the edges. A digitally enhanced images of the rings is shown in Figure 4.7.

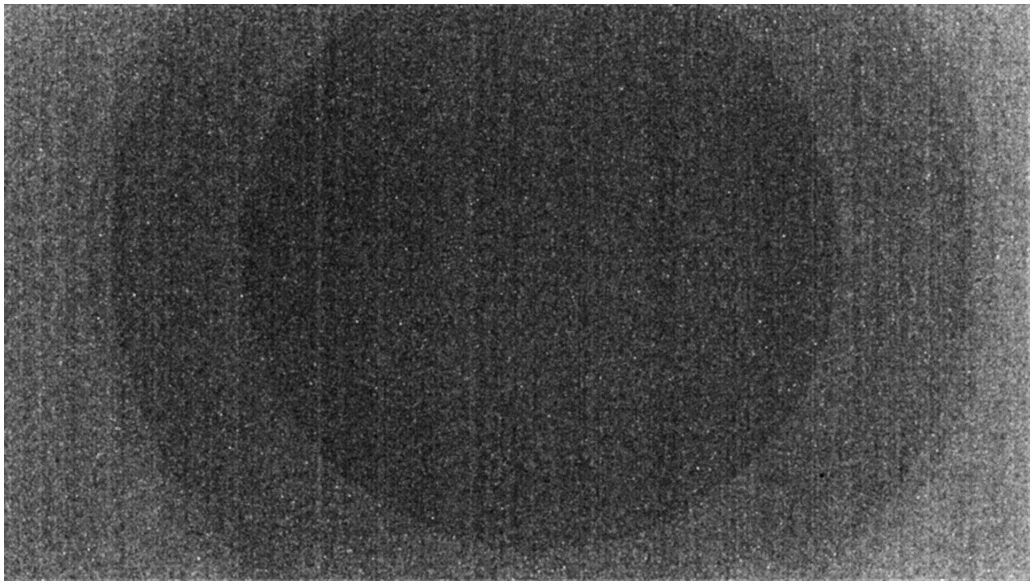

Figure 4.7: An image acquired by the RF-WC1080P1 webcam with its lens removed, showing the artifacts introduced by the flat field correction.

After excluding different theories for the cause of these artifacts - among which image compression or optical effects of the cover glass where considered - a flat-field correction introduced by the SPCA2281B3 web cam controller was identified as the likely culprit. Flat-field correction - or flat fielding - is the process by which a digital camera compensates for systematic errors in pixel brightness or gain. While these errors also include pixel-to-pixel differences caused by variations in the CMOS amplifiers, these are usually compensated on-chip by the image sensor itself based on a calibration done by the manufacturer - as explained in Chapter 3.2 [34].

The most dominant effect that the camera itself has to compensate for is the difference in image brightness caused by optical vignetting. This effect describes the gradual decrease in light intensity towards the periphery of a camera lens' field of view. As light enters the lens at increasingly steep angles, it is partly blocked by the casing of the lens itself - thus reducing the received light intensity at the sensor. Also - due to fundamental optics - the light flux received by an image film or sensor is reduced by the fourth power of the cosine of the light ray's angle relative to the optical axis of the lens. These effects combine to produce a falloff in brightness towards the edges of the frame. Since this kind of vignetting depends on the optics used, the sensor itself cannot compensate for it but has to rely either on the camera controller or the computer software to weigh the pixels accordingly in order to cancel out this effect [35].

In this case, it is suspected that the web cam controller applies a slightly different

digital gain to each pixel depending on its distance to the optical center. Since optical vignetting causes the edges of a frame to receive less light, this is where the controller would apply the most additional gain. Because no lens is used in these experiments, the correction would artificially increase the brightness towards the periphery - matching the observations.

Camera Parameters

The webcam controller allows for a range of camera parameters to be set via USB. (Table 4.2) While the range of values these parameters can take is documented, their units and functions are not. Therefore, a considerable amount of automated trial-and-error testing had to be performed to optimize these parameters for maximum low light performance.

Parameter	min. Value	max. Value
Effective		
brightness	0	255
contrast	0	95
white balance temperature auto	0	1
white balance temperature	2800	6500
exposure auto	0	3
gain	16	255
No Effect		
saturation	0	100
hue	-2000	2000
power line frequency	0	2
backlight compensation	8	200
exposure absolute	3	8192
gamma	100	300
sharpness	0	70

Table 4.2: The list of adjustable parameters for the RF-WC1080P1 webcam provided by the V4L2 drivers. No further documentation was available and not all parameters appeared to have an effect.

As a result of these tests it was found that the parameters displayed in the lower portion of Table 4.2 did not have any effect on the sensor's monochrome sensitivity. In the case of some parameters (i.e. saturation, hue, ...) this is perfectly logical as one would expect them to only affect the color component of an image. For others - especially the parameter "exposure absolute" - the lack of influence on the acquired signal is puzzling.

One would expect the "exposure auto" setting to switch between different modes of automatic or manual exposure time control - which to some extent is true. However, no setting of this parameter seemed to take the value of "exposure absolute" into account. This was especially unfortunate since the increase of exposure time was expected to yield a strong improvement in signal to noise (S/N) ratio.

The "gain" parameter seemed to behave much like one would expect the analogue gain of a CMOS sensor to do - increasing both the signal and noise in the images. It is suspected that the "brightness" parameter constitutes a type of digital gain that is applied to the image after digitization. Although a digital gain will increase the brightness of a frame, there is no advantage to be gained regarding the S/N ratio. Therefore this parameter was left at its default value. Finally, also the "white balance temperature" was observed to have a noticeable influence on image signal. This could be explained by considering the color of the LED (and by extension that of the phosphor). At 470 nm the diode emits a deep blue color, which resembles a light source with a very high color temperature. By - for example - setting the white balance temperature of the camera to its maximum value of 6500 (Kelvin, presumably), it will try to display the color of light emitted by a 6500 K light source as white. Since only the brightness values of the frames are considered, this translates into a stronger signal for light towards the blue end of the spectrum. These corrections are of course also done by the webcam controller and therefore constitute digital enhancements of the signal - which should be avoided at this stage. However, since the white balance correction cannot be turned off - only set to automatic - the value of this parameter was increased to the maximum.

Light Sensitivity

After extensive testing, the lowest detectable light flux of the RF-WC1080P1 was found to be around $2 \cdot 10^8$ Photons/s/mm^2. Figure 4.8 shows a plot of the sensor's signal intensity versus incoming photon flux. The camera parameters used to acquire this data are listed in Table 4.3. The setup for this experiment consisted of a 1 mm thick wire that was placed close to the image sensor inside of the test chamber. The shadow cast by the wire onto the sensor results in a dark area on the frames which was used to measure the noise. By subtracting the average pixel value of the dark area from the average pixel value of the illuminated portion of the frame, the generated signal could be calculated.

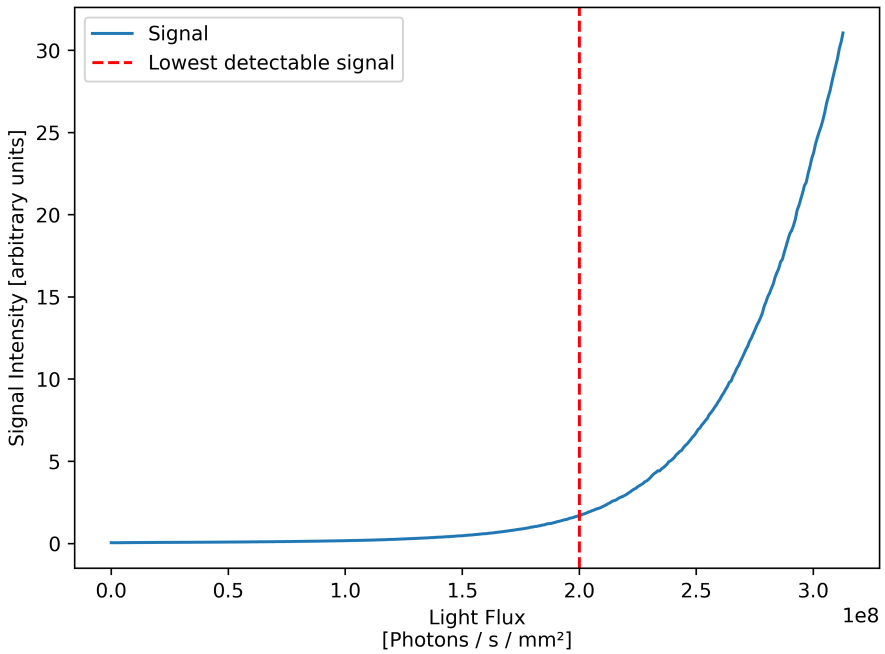

Figure 4.8: Signal intensity as a function of light flux using the RF-WC1080P1 camera. The signal value was acquired by only illuminating part of the frame and subtracting the mean pixel values of the dark areas from those of the bright areas. The threshold for a detectable signal was found to be around $2 \cdot 10^8$ Photons/s/mm^2.

Influence of Temperature

The datasheet of the OV2735 image sensor specifies that a stable image can be produced in a temperature range between 0 to 60 °C. In order to investigate how the signal strength and image noise change within that range, the test setup was modified so as to facilitate a thermocouple and two power resistors glued to the edge of the image sensor. The entire setup was then moved into a fridge set to a temperature of 2 °C. Because of the waste heat generated by the device itself, this yielded a lowest reachable temperature of 15 °C at the sensor. By passing an adjustable current trough the power resistors, the sensor temperature could be raised up to 80 °C.

Using this setup, a sweep of the temperature range was performed while the sensor was illuminated by the LED. The amount of signal recorded versus the sensor temperature is shown in Figure 4.9. Above 59 °C no image was produced and the camera returned an array of white pixels. From these tests it was concluded that for maximum sensitivity the sensor should be operated below 45 °C.

Parameter	Value
brightness	135
contrast	95
white balance temperature auto	0
white balance temperature	6500
exposure auto	1
gain	255

Table 4.3: Values of the camera parameters used to achieve the highest light sensitivity. These parameter values were used to acquire the data shown in figure 4.8.

4.4.2 Sony IMX219

Parameters

The sensor parameters of IMX219 can be configured by setting a wide range of internal sensor registers via an I^2C bus. While there are hundreds of registers that manage different aspects of the acquisition and readout process, the focus of this chapter will be on a subset of 11 settings that were most relevant to the sensor's low light performance. (Table 4.4) Each register is identified via a unique address of four hexadecimal digits and can be set to a value between 0 and 255, also represented in hexadecimal. Where necessary, two consecutive registers can be interpreted as one, resulting in a range of values between 0 and 65535. To improve readability in such cases, only the address of the first register will be listed here forth.

Gain

The very first parameter listed - "ANALOGUE_GAIN_GLOBAL_A" - corresponds to the analogue gain that is applied to each pixel's readout stage. For this parameter the datasheet specifies a maximum value of 232. The actual amplification factor that is applied to the pixels is given by the following expression

$$Amp.\ Factor = \frac{256}{256 - X}$$

where X is the value of the register "ANALOGUE_GAIN_GLOBAL_A". This transformation allows for very fine control at lower gains and results in increasingly larger steps at higher gains. At the maximum specified value of $X = 232$, this results in an amplification factor of 10.66. That being said, there is no mechanism or check in

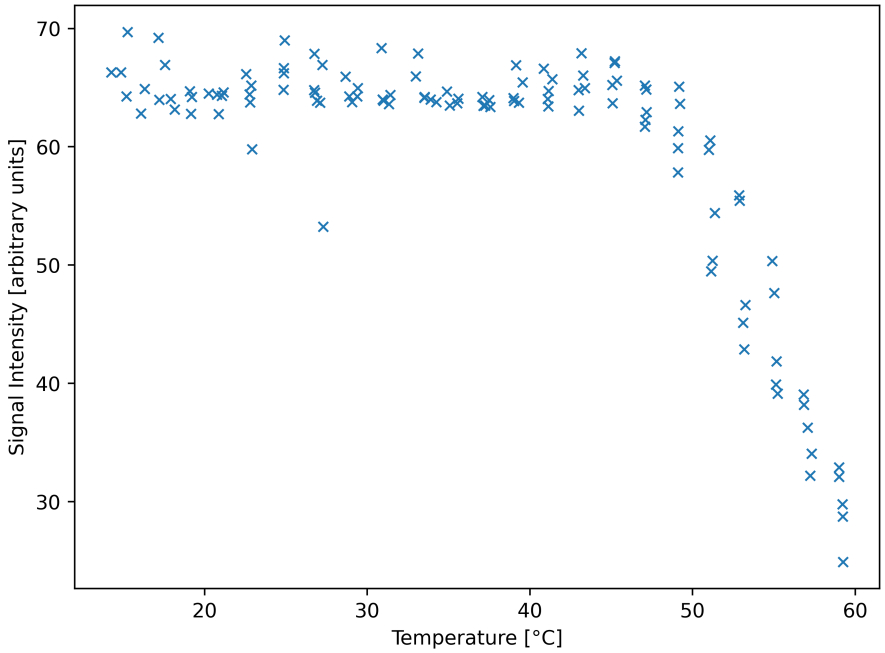

Figure 4.9: Signal intensity recorded by the OV2735 sensor exposed to a fixed light flux as a function of sensor temperature. The signal is roughly constant up until a temperature of 45° and then declines sharply as the temperature increases.

place that will hinder to user to increase the register's value to the theoretical maximum of 255. After some experimentation it was found that the amplification factor does in fact continue to increase up until a value of $X = 254$. (Figure 4.10) Furthermore, the amplification factor could be observed to increase the signal in a linear fashion up until a value of $X = 253$ - corresponding to an amplification factor of 85.33.

The parameter "DIGITAL_GAIN_GLOBAL_A" can be used to set an amplification factor that is applied by the sensor itself after digitizing the signal. Again, this type of amplification will not yield any increase in S/N ratio so it was left disabled.

Sensor Clock and Exposure Time

Another variable that was expected to drastically influence the low light performance was the sensor's exposure time. It is influenced by many different sensor parameters and can - according to the datasheet - be calculated by

$$Exp.\ Time = (CIT \cdot \frac{LL}{2} + 500) \cdot \frac{1}{PCF}$$

Parameter Name	Parameter Address	Typical Value
Gain		
ANALOGUE_GAIN_GLOBAL_A	0157	FE
DIGITAL_GAIN_GLOBAL_A	0158	0100
Exposure Time		
COARSE_INTEGRATION_TIME_A	015A	1000
FRAME_LENGTH_A	0160	FFFF
LINE_LENGTH_A	0162	FFFF
Clocking		
PREPLLCK_VT_DIV	0304	03
PREPLLCK_OP_DIV	0305	03
PLL_VT_MPY	0306	002B
PLL_OP_MPY	030C	0055
VTPXCK_DIV	0301	05
OPPXCK_DIV	0309	0A

Table 4.4: The parameters that were found to influence the light sensitivity of the IMX219 sensor. They can be divided into managing three different aspects of the acquisition: analogue gain, exposure time and clock speed.

where CIT is COARSE_INTEGRATION_TIME_A, LL is LINE_LENGTH_A and PCF is the pixel clock frequency - which in turn is given by

$$PCF = \frac{SICF \cdot PLL\_VT\_MPY}{VTPXCK\_DIV \cdot PREPLLCK\_VT\_DIV}$$

where SICF is the sensor's input clock frequency - which in case of the Raspberry Pi Camera Module V2 is $SICF = 24\ MHz$.

To sum up, the exposure time is directly influenced by the parameters COARSE_-INTEGRATION_TIME_A and LINE_LENGTH_A – and can indirectly be influenced by changing the internal clock frequency of the sensor. Figure 4.11 shows a block diagram of the sensor's internal clock system. The relevant clock for influencing the exposure time is labeled "PIX_CLK" in this diagram. As can be gathered from Figure 4.11, the pixel clock is generated by first dividing the input clock frequency using "Pre-Div 1", then multiplying it using the phase-locked loop 1 ("PLL 1") and then dividing it again via "DIV 1". All of these dividers and multipliers can be configured through their corresponding registers from Table 4.4 and have respective minimum and maximum values listed in the datasheet. According to the specified limits of all the relevant parameters, the maximum exposure time can be calculated to be 26.8 s (at an input clock frequency of 24 MHz).

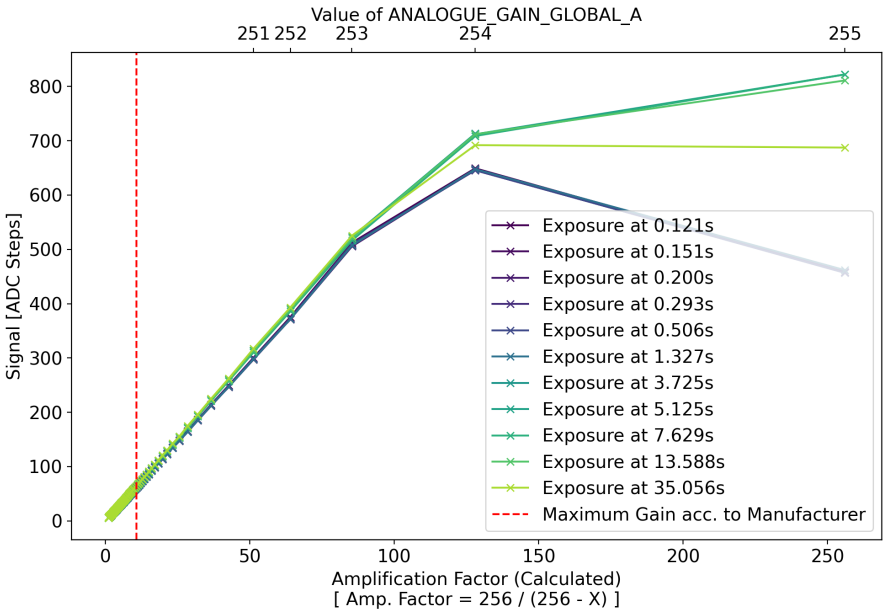

Figure 4.10: Signal produced by the sensor at varying amplification factors and different exposure times. The brightness of the LED used to provide the reference illumination was adjusted relative to exposure time in order to keep the signal intensity within ADC range. It can be seen how the linearity of the sensor worsens when operating above the parameter range specified by the manufacturer and is completely lost around one order of magnitude above it.

However - similarly to the analogue gain - it is possible to exceed the specified limits of these registers and so extend the functionality of the sensor. By decreasing the multiplication factor of "PLL 1", it was possible to under-clock the pixel readout system and thereby drastically increase the exposure time. By extensive trial and error testing it was found that the lower limit of the pixel clock is actually set by another frequency - that of the output clock, which is responsible for transferring the pixel data via the CSI. It too has a set of dividers and multipliers that can be similarly configured. Therefore it was possible to also reduce the output clock's frequency, allowing the pixel clock to be slowed down even further. By employing these measures it was possible to increase the maximum exposure time to 167 s (register values shown in Table 4.5).

Similarly to the gain parameter, the exposure time was found to increase the signal in a very linear fashion over most of its range. (Figure 4.12)

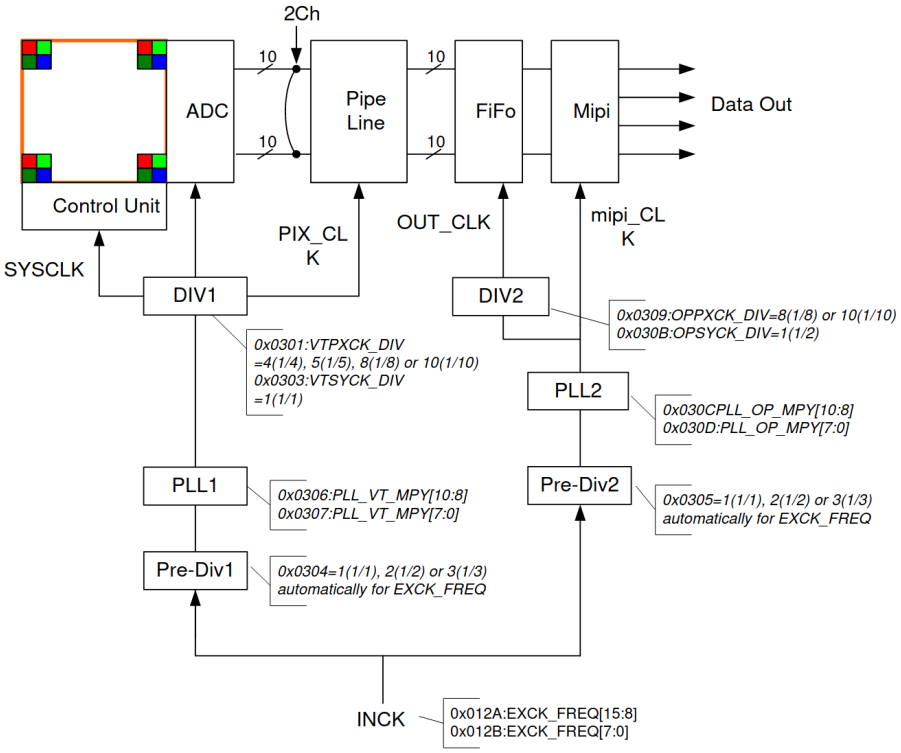

Figure 4.11: Block diagram of the IMX219's clock system showing the interconnectedness of the exposure timing and the data transfer clock. By changing the relevant register values, the different clock frequencies could be adjusted to achieve very high exposure times.

Bayer Filter

As previously outlined in Section 3.2, the acquisition of color images requires an image sensor to feature some sort of color filter on top of its pixel array. These color filters are produced by successively depositing layers of photoresist and usually feature a thickness in the micrometer range. Photoresist chemicals typically consist of a polymer resin that undergoes structural changes when exposed to certain frequencies of light. The alterations within the exposed areas of the resin make it either more or less (i.e. negative or positive photoresist) susceptible to chemical attack, which allows the coating to be selectively dissolved in a subsequent washing step. A positive photoresist commonly used for color filter arrays is Diazonaphthoquinone(DNQ)-novolac [36]. A microscope image of the IMX219 (Figure 4.13) clearly shows the classic Bayer pattern on top of the pixel array.

For the planned measurement of low-energy positrons however, having this layer of polymer color filter on top of the photosensitive area is undesirable. As the filter functions on the principle of color subtraction, it effectively reduces the intensity of

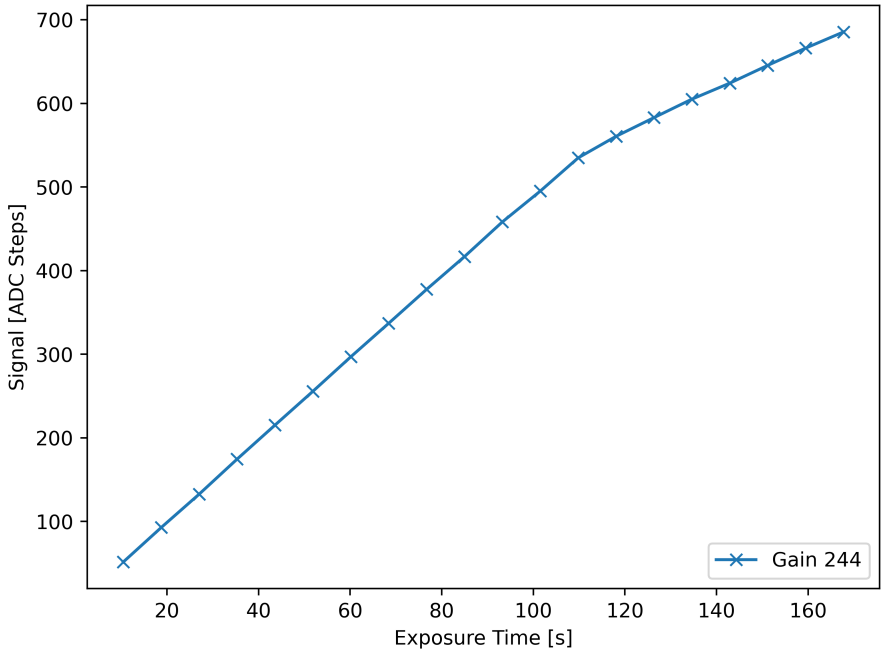

Figure 4.12: Signal produced by the sensor being exposed to a constant illumination source, as a function of the exposure time. The area of linearity extends beyond the values allowed by the manufacturer's specifications, but tapers off above 110 seconds of exposure time.

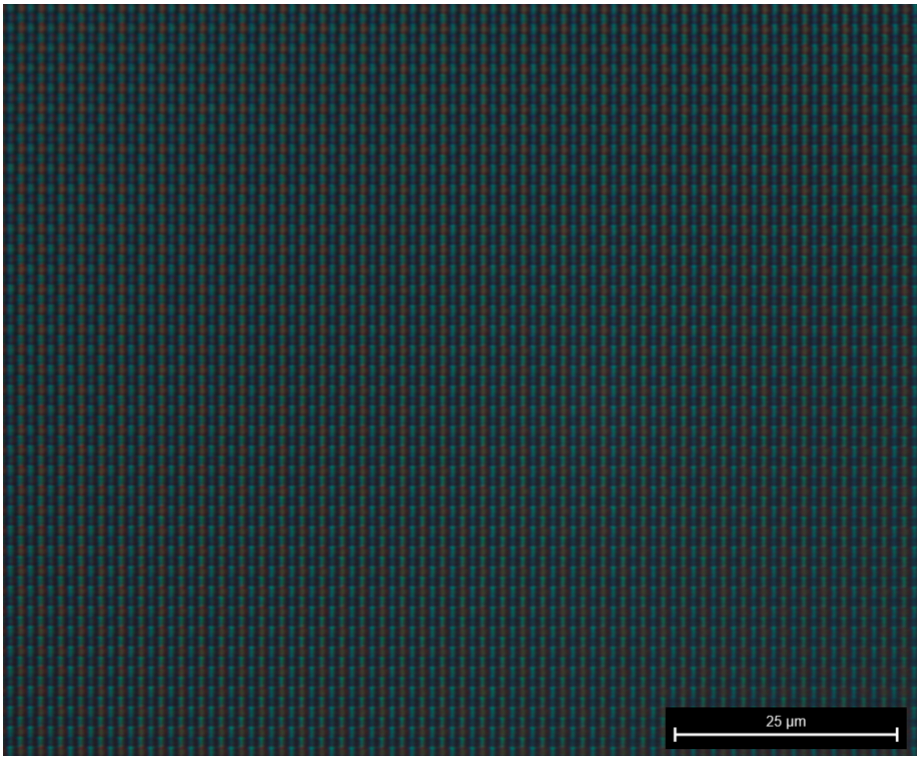

Figure 4.13: Microscope image of the IMX219's pixel array. The color filter - here a classic Bayer pattern - is clearly visible.

Parameter Name	Parameter Address	Value
Exposure Time		
COARSE_INTEGRATION_TIME_A	015A	FFFC
FRAME_LENGTH_A	0160	FFFF
LINE_LENGTH_A	0162	FFFF
Clocking		
PREPLLCK_VT_DIV	0304	03
PREPLLCK_OP_DIV	0305	03
PLL_VT_MPY	0306	0008
PLL_OP_MPY	030C	000D
VTPXCK_DIV	0301	05
OPPXCK_DIV	0309	0A

Table 4.5: Register values of the IMX219 used to achieve 167 second long exposures.

incoming light. A perfect Bayer filter - in which only one quarter of the pixels receive blue light - would attenuate the signal of the 470 nm phosphor emission by 75%. Further, when directly implanting low-energy positrons into the image sensor, the particles would deposit most of their energy within the filter layer - thus also strongly attenuating the signal. Therefore, a method to remove the color filter - and by extension the microlens array - was required.

In their efforts to convert a different version of the Raspberry Pi camera module into an ultraviolet imaging system, Wilkes et al. used a dedicated photoresist stripping solution to remove the color filter of their sensor [37]. The chemical used is a product by DuPont sold under the name Posistrip EKC830. However, since this product was not commercially available in quantities smaller than 50 L, a different approach had to be taken.

The material safety data sheet (MSDS) of the EKC830 chemical specifies that it is comprised of a proprietary mixture of N-Methyl-2-pyrrolidone (NMP) and 2-(2-Aminoethoxy)ethanol (AEE). While it would have been possible to simply purchase those chemicals and proceed to dissolving the color filter using a mixture of the two, it was decided to first test a range of more commonly available solvents. This was done in the hope of avoiding the use of NMP, which is currently being phased out of industrial use due to concerns about its environmental impact [38]. To that end the solvents listed in Table 4.6 have been tested by submerging the IMX219 into an magnetically stirred bath of the solvent at elevated temperatures.

Tested Solvents
Ethanol
Acetone
Isopropanol
Toluene
Methanol
Cyclohexane
DMSO
Dichloromethane
Trichloromethane
MELLERUD Glue Remover
1M Sodium Hydroxide
1M NaOH + Isopropanol
Trichlorobenzene
Fuming Nitric Acid

Table 4.6: Solvents tested for removing the color filter off of the IMX219 image sensor. Aqueous solutions of Sodium hydroxide as well as concentrated nitric acid were able to attack the color filter; however not without also destroying the sensor in the process.

After extensive testing it was found that only concentrated sodium hydroxide solutions and nitric acid had a visible effect on the color filter. Submerging the sensor in a bath of a one molar solution of NaOH led to the filter slowly peeling away from the Silicon substrate over the course of an hour. By submerging the entire sensor however, the NaOH also attacked the bonding wires and copper traces that connect to the Silicon dye - thus rendering this process unusable. Some success has been observed by carefully placing single drops of nitric acid in the center of the image sensor where it would not come into contact with the bonding wires or the circuit board. Ultimately however, this method was found to be too unreliable and the chemicals needed for recreating the EKC830 solution were purchased.

The sensor was again submerged into a stirred bath of the solvent - in this case 50% (v/v) NMP and 50% AEE - and left for some time at elevated temperature. While the color filter did not entirely dissolve on its own, it could be removed by lightly brushing the surface of the sensor with a cotton swab. After the initial removal a fresh bath of the solution was prepared in order to wash away any remaining residue. Figure 4.14 shows a microscope image of an area in which the color filter was only partially removed. The transition and difference in appearance of the pixel array with and without filter are clearly visible.

The de-bayered sensor was then characterized using the LED test setup and a 2.5 fold

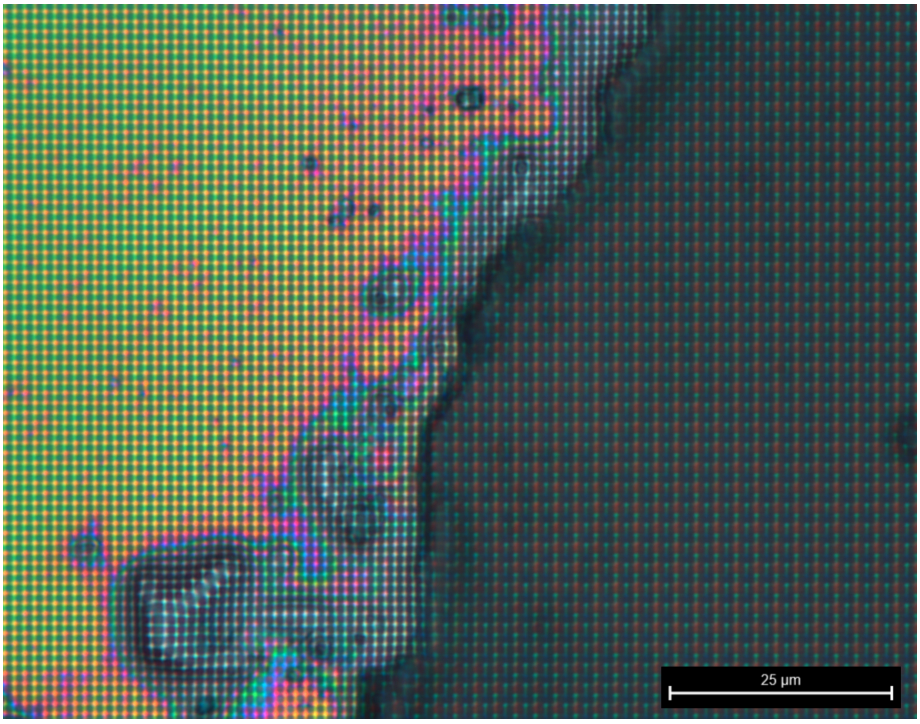

Figure 4.14: Microscope image of the transition from color filter to bare sensor array at the edge between an area of the sensor in which the Bayer filter has been removed and a yet untreated area.

increase in sensitivity to 470 nm light was observed. This value can be compared to the spectral sensitivity that the datasheet specifies for the sensor. (Figure 4.15) From this graph it can be gathered that at a wavelength of 470 nm the color filter transmits roughly

$$80\% \ (for\ blue\ pixels)$$

$$20\% \ (for\ green\ pixels)$$

$$4\% \ (for\ red\ pixels)$$

of the incoming light. In the knowledge that the color filter features a classic Bayer pattern with 25% blue, 25% red and 50% green pixels, the total light transmission for the whole pixel array at 470 nm can be calculated to be

$$\frac{1}{4} \cdot 80\% + \frac{1}{2} \cdot 20\% + \frac{1}{4} \cdot 4\% = 31\%$$

One would therefore expect to see an increase in sensitivity by a factor of $\frac{1}{31\%} \simeq 3.2$ after removing the color filter.

However - as stated previously - modern image sensors also commonly feature an

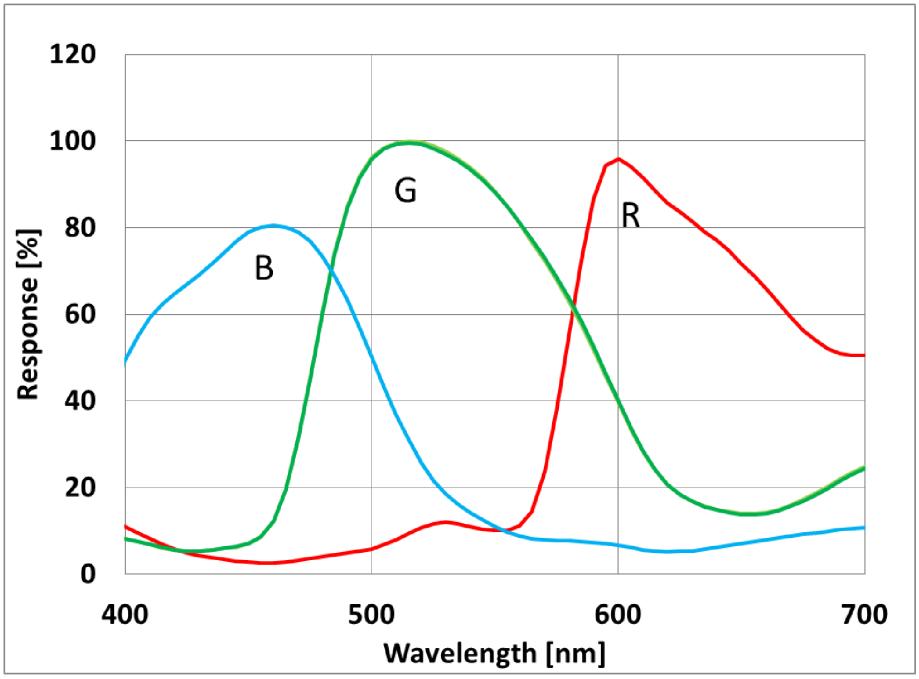

Figure 4.15: Normalized spectral sensitivity of the sensor - neither lens characteristics nor light source characteristics included. Image from [39]

array of micro lenses on top of the color filter that help to utilize all of the incoming light by focusing it onto a smaller area within the pixel that is entirely photosensitive. Without the effect of the lenses, part of the incoming light will fall onto the surrounding structure and will therefore not be detected. The discrepancy between the measured and expected light sensitivity could therefore be explained by the lack of micro lenses after the removal process. If one assumes that the lenses where perfectly able to redirect all of the light onto the sensitive area, the ratio of photosensitive area to total pixel area could be calculated by dividing the actual increase in sensitivity by the expected increase of sensitivity. In this case equating to

$$\frac{2.5}{3.2} \simeq 78\%$$

Light Sensitivity

After observing the sensor's very linear response in sensitivity to both amplification factor and exposure time (Figure 4.10 and 4.12) it was concluded that it is reasonable to determine the light sensitivity at a standard exposure time and gain setting and to then linearly interpolate the calibration for any other given sensor setting. This model would be valid up to an exposure time of 100 s and a gain setting of 253. When using sensor

settings beyond these values the nonlinearities that can be observed in Figure 4.10 and 4.12 have to be taken into account.

The standard sensor settings at which the light sensitivity would be defined were set at 1 second of exposure time and 1x (0 dB) gain. At these settings, the IMX219 (with its color filter and micro lens array removed) has been found to require a light flux of around 20 photons per second per pixel at 470 nm to generate a signal of 1 LSB (Least Significant Bit - the smallest difference resolvable by the internal analogue to digital converter).

While the datasheet does specify a value for light sensitivity, the descriptions of the test condition used are lacking the necessary information required to calculate the light flux at the sensor's surface. At best an upper limit of 136 photons per second per pixel (at a color temperature of 3200 K and with the color filter in place) required for 1 LSB can be computed from the data provided.

Noise

In order to compute the signal to noise ratio that can be expected when performing the positron measurement, the dark noise of the sensor had to be characterized. This could be done by simply using the preexisting test setup without the LED - thus operating the sensor in complete darkness. As a measure for the image noise, the standard deviation of a given pixel over ten consecutive frames was considered. This value was calculated for every pixel and then averaged over the entire frame to compute the mean pixel noise. The measurement was then repeated for different exposure times and gain values.

In order to enable the comparison of the measured noise between different exposure times, a fixed integration time had to be defined. If - for example - the total integration time is set to 100 s, the noise calculated from a series of frames acquired at 100 s of exposure time can be plotted as is. If one then measures the noise from a series of frames with 10 s of exposure, the difference in total integration time has to be taken into account before comparing the two data points. In 100 s of integration time, 10 frames of 10 s each could have been obtained, and subsequently averaged.

Since the sum of random noise scales with the square root of the number of samples N, the sum of a series of samples X_n consisting of random noise with the same amplitude is

$$\sum_{n=1}^{N} X_n = X_0 \cdot \sqrt{N}$$

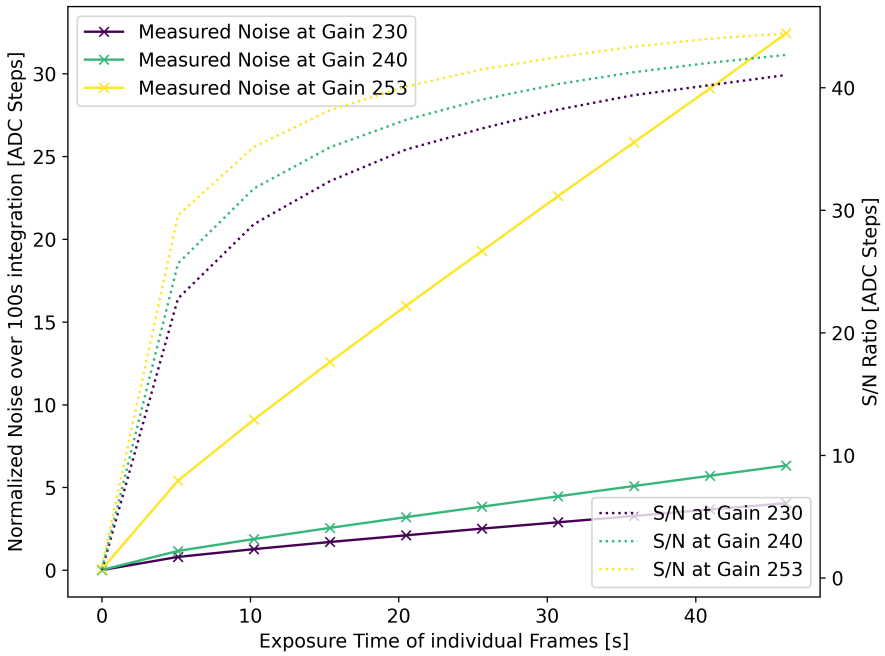

Figure 4.16: Dark noise of the IMX219 measured at different exposure times and gains and normalized to 100 s integration time, showing the sub-linear increase of it as a function of the exposure time. From these results it can be gathered that the sensor noise does in fact decrease with longer exposure time, even when compensating for the increased acquisition time.

The average of such a series of data points is therefore

$$\frac{X_0 \cdot \sqrt{N}}{N} = \frac{X_0}{\sqrt{N}}$$

In order to compare the amount of noise in a frame at 100 s exposure with the amount of noise in a frame at 10 s exposure, the value obtained from the 10 s frame has to be divided by $\sqrt{\frac{100s}{10s}}$.

Figure 4.16 shows the dark noise measured for different gains and exposure times and normalized to 100 s of total integration time. Using the assumption that the light sensitivity scales linearly with gain and exposure time - as stated above - and assuming a 1 to 10.000 conversion factor from positrons to photons within the phosphor at an implantation energy of 10 kV, the expected signal to noise ratio can be calculated and is plotted in Figure 4.17. From these plots it can be gathered that the S/N does continuously increase with exposure time. At very long exposures however, the values seem to level off and provide diminishing returns.

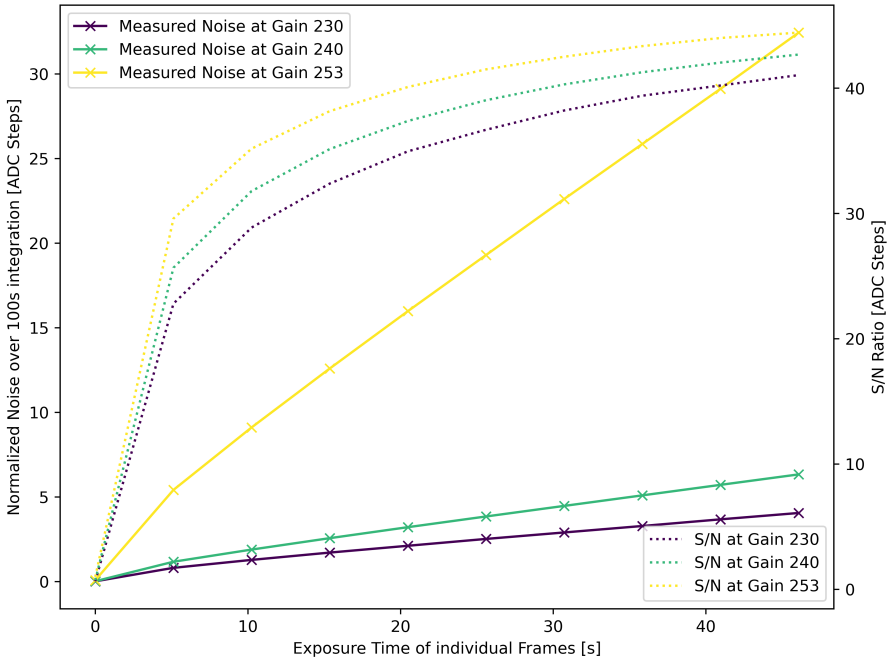

Figure 4.17: Expected S/N ratio using phosphor at 10 keV *positron energy at different exposure times and gains and normalized* 100 s *integration time. Due to the disproportionately lower noise at higher exposure times, the S/N ratio can be observed to continuously increase.*

Influence of Temperature

Regrettably - due to time constraints - it was not possible to fully characterize the influence of temperature on the IMX219. The data sheet specifies a maximum operating temperature of 60 °C - identical to that of the OV2735. It was therefore assumed that the behavior at elevated temperatures would be similar to that of the previous sensor - being a consequence of the CMOS technology employed to manufacture both sensors.

The IMX219 features an internal temperature probe that can be activated and read via the I^2C bus. By setting the highest order bit of the register with address "0140", the temperature sensor can be enabled and its value read from the remaining bits of the same register. In theory the probe features an operating range between -10 and 95 °C and a resolution of ± 5 °C. During the characterization and the measurements with positrons the values of this sensor where always recorded and provided useful feedback on the operating conditions of the device.

4.4.3 Sony IMX477

The IMX477 - as featured in the Raspberry Pi HQ camera module - offers various advantages over the previous sensor. At over 12 megapixels its active area is noticeably larger than that of the IMX219. Furthermore, it uses a 12-bit ADC to digitize the analogue pixel values, translating to a 4x increase in color depth. Also, its ability to synchronize the frame acquisition to an external clock allows for arbitrarily long exposure times.

Parameters

A major difficulty in characterizing this sensor was the absence of documentation for its register map. While the datasheet is publicly available, the appendices that contain the relevant information are not. Therefore, the addresses and functionalities of the most important registers had to be gathered from different online sources and in some cases reverse engineered by monitoring the sensors I^2C communication with the raspiraw drivers.

Ultimately, the registers listed in Table 4.7 were identified as relevant and their range of values tested. Again, each registers is identified by a four digit hexadecimal address and can store values ranging from 0 to 255. Where two successive registers are combined into one value, only the address of the first register is listed.

Parameter Name	Parameter Address	Typical Value
Gain		
ANALOGUE_GAIN_GLOBAL	0204	03FF
DIGITAL_GAIN_GREEN	020E	0100
DIGITAL_GAIN_RED	0210	0100
DIGITAL_GAIN_BLUE	0212	0100
DPGA_USE_GLOBAL_GAIN	3FF9	01
Exposure Time		
COARSE_INTEGRATION_TIME	0202	1000
LINE_LENGTH_PCK	0342	FFFF
SHIFT	3100	00

Table 4.7: The relevant registers influencing the light sensitivity of the IMX477. Again, analogue gain – controlled by the parameter ANALOGUE_GAIN_GLOBAL – and exposure time – influenced by COARSE_INTEGRATION_TIME, LINE_LENGTH_PCK and SHIFT – are the most influential factors.

Gain

The parameter "ANALOGUE_GAIN_GLOBAL" again controls the analogue gain applied to each pixel. For the IMX477 the allowed values range from 0 to 1023 and are translated into the actual amplification factor via the expression

$$Amp.\ Factor = \frac{1024}{1024 - X}$$

where X is the value of "ANALOGUE_GAIN_GLOBAL". Since in this case two registers are combined into one, the value of "ANALOGUE_GAIN_GLOBAL" could be increased even further, up to 65535. However, any values above 1023 result in the sensor becoming unresponsive and needing to be power-cycled - likely due to the nonsensical results of the above equation for X > 1023.

In case of the digital gain, the IMX477 allows for setting individual values for the differently colored pixels, corresponding to the registers "DIGITAL_GAIN_GREEN", "DIGITAL_GAIN_RED" and "DIGITAL_GAIN_BLUE". Alternatively, the register "DPGA_USE_GLOBAL_GAIN" can be set which overwrites the individual gains and applies the value of "DIGITAL_GAIN_GREEN" to every pixel. For all of the following experiments, the digital gain of the sensor was left disabled.

Hardware Synchronization and Exposure Time

While this information cannot be regarded as definitive, different tests and analysis of the raspiraw software indicate that the exposure time of IMX477 is given by

$$Exp.\ Time = T_{line} \cdot (CIT + \frac{FIT}{LLP})$$

where CIT is the value of "COARSE_INTEGRATION_TIME", FIT is the fine integration time - a constant with value 1936 - and LLP the value of "LINE_LENGTH_PCK". T_{line} in turn is given by

$$T_{line} = \frac{LLP}{IVTPXCK \cdot 4}$$

where IVTPXCK is the frequency of the internal image processing clock, found to be equal to 250 MHz. Finally, the register "SHIFT" can be used to multiply the value of "COARSE_INTEGRATION_TIME" via the relation

$$CIT_{after} = CIT_{before} \cdot 2^{SHIFT}$$

thus being able to drastically extend the exposure time. Using these registers at their maximum allowed values results in an exposure time of 550 s. It is strongly suspected that this number could be increased even further by slowing down the internal image processing clock - similar to the approach take with the IMX219. However, in the limited amount of time available it was not possible to correctly identify the relevant registers for influencing the clock's frequency.

In any case, another feature of the IMX477 may offer even greater improvements in exposure time. For the use in stereoscopic or similar cameras setups, the sensor offers the possibility to synchronize its frame acquisition to an external clock signal. That way, two or more camera sensors can be configured to capture their frames at the exact same time. By extension, this mode could also be used to acquire frames with arbitrarily long exposure times by providing a sufficiently slow external clock signal. This technique has been developed and documented on the official Raspberry Pi forum by the user "HermannSW", who we would like to recognize and thank at this point for his great contributions to the open-source community in regards to this sensor.

By using a modified version of the raspiraw driver and an inverter IC plus voltage divider for signal conditioning, it is possible to use the Raspberry Pi itself to provide the external clock signal needed for acquiring long exposures in this manner. This technique was successfully replicated and indeed enabled the acquisition of frames with arbitrarily long exposure times.

Temperature Sensor

Similarly to the previous sensor, the IMX477 also features an internal temperature probe that can be accessed via the I^2C bus. Setting the least significant bit of register "0138" enables the sensor and allows the temperature value to be read from register "013A". Due to lack of proper documentation the range and resolution of this measurement are unknown.

4.4.4 Conclusion

After extensively testing the three available sensors a quite clear conclusion could be drawn. While the OV2735 on its own is certainly a capable sensor, the thick glass cover and the limited amount of fine control allowed by the webcam controller make the RF-WC1080P1 webcam entirely unsuitable for this experiment.

The Sony IMX219 - as part of the Raspberry Pi camera module V2 - offers very low level interfacing capabilities and has been demonstrated to perform exceptionally well even when operated far outside its specified limits. Further, the small form factor of the camera module itself will allow for more flexibility in the subsequent design of the experimental setup within the positron beam.

Regrettably, it was not possible to extensively characterize the performance of the IMX477 due to time constraints. However, the preliminary tests and the information gathered online indicate that this sensor too offers great versatility and the potential to perform extremely sensitive measurements. While the considerably larger size of the corresponding Raspberry Pi camera module would have made the integration into the experimental setup somewhat more challenging, the benefits resulting from a larger pixel array and higher amplification factor would certainly outweigh the added complexity. To unlock the sensor's full potential however, having access to the complete datasheet is definitely necessary.

Ultimately, the IMX219 was chosen as the most promising candidate for the measurement with positrons.

5 Experimental Setup for the Positron Measurement at a Laboratory Beam

5.1 Laboratory Beam Overview

The measurements of this thesis were performed using a radioisotope based positron beam - hereafter referred to as the Lab-Beam. The setup was originally constructed to perform positron induced Auger-electron spectroscopy and has been converted and upgraded in 2020 to be able to perform Doppler-Broadening Spectroscopy (DBS). It features a ^{22}Na positron source, electromagnetic beam guidance and a sample chamber equipped with two high resolution germanium detectors. Figure 5.1 shows a schematic overview of the Lab-Beam.

The positrons emitted by the ^{22}Na source feature a continuous spectrum of energies and have to be moderated by a thin tungsten foil in order to form a monoenergetic beam. The low-energy positrons re-emitted by the moderator are then accelerated and adiabatically guided towards the sample chamber. This is achieved by driving a number of magnetic coils placed around the outside of the beam line and applying a voltage potential between the moderator foil and the target sample. In Figure 5.1 the different types of coils are abbreviated with S for solenoids, H for Helmholtz pairs, F for flange coils and K for correction coils. In order to filter out any unwanted decay particles, the beam is guided around a 90° bend before arriving at the sample chamber. By varying the voltage bias between moderator and sample, the positron energy can be adjusted - typically in the range of 0 to 30 keV [40].

The sample chamber of the Lab-Beam consists of a CF 100 six-way crosspiece, in which two of the flanges are occupied by the cylindrical germanium detectors, one connects to a turbo-molecular pump, the front is covered by a blind flange and the sample to be tested is inserted from below - placed on a specially made sample holder. The positron beam is guided into the chamber from above. Figure 5.2 schematically shows the crosspiece as seen when standing in front of the Lab-Beam. The standard sample holder that is

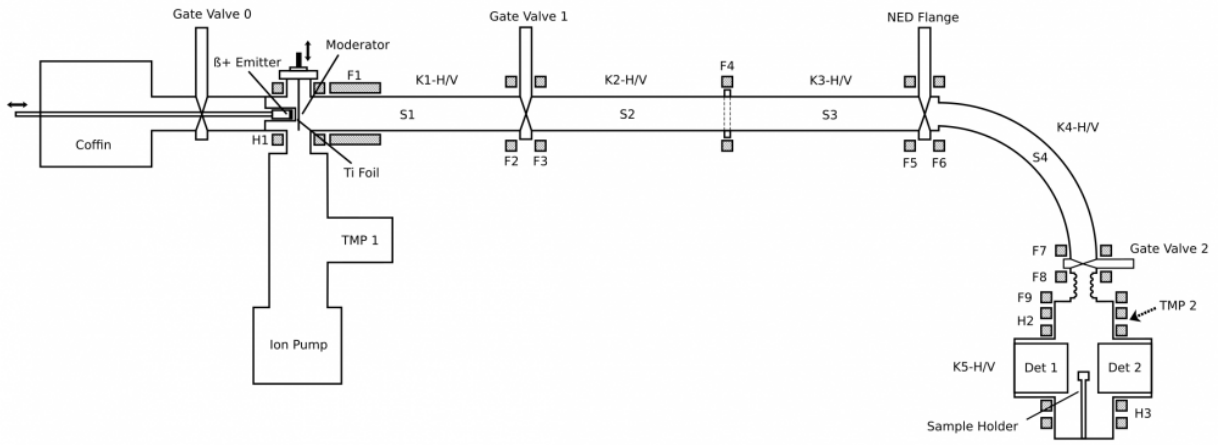

Figure 5.1: Schematic drawing of the Lab-Beam setup. The types of coils are abbreviated with S for solenoids, H for Helmholtz pairs, F for flange coils and K for correction coils. Image from [40]

used when performing DBS measurements with this setup consists of a ferromagnetic rod on top of which the material of interest is placed. To provide electrical isolation this rod is in turn mounted on an insulating plate made from plastic. The entire setup is built onto a CF 100 blind flange that features a high voltage passtrough in its center. In Figure 5.3 a sketch of the standard sample holder is shown - with the material to be analysed positioned in the middle of the chamber in between the protruding germanium detectors.

The detectors consist of a large germanium crystal, carefully doped to form a macroscopic PIN diode structure that are - in combination with very sensitive readout electronics - able to count the number and energy of incoming γ-photons. In this context, the photons are produced by the annihilation reaction of the positrons within the sample material. An electron-positron annihilation reaction predominantly produces two γ-photons with an energy of 511 keV each. By measuring the slight deviations in energy from the expected value of 511 keV, information about the electronic structure and thereby the material properties of the sample can be inferred. This is the basis of Doppler-Broadening Spectroscopy [5].

At this point it shall be mentioned that while the use of DBS was not actually required to perform this experiment, the detectors were part of the preexisting setup and could therefore be used without additional effort to acquire DBS data in parallel to the main objective of detecting the beam using the image sensor itself.

One of the most crucial factors for the success of the planned experiment is the available positron flux at the sample location. It is dependent on different factors like the activity

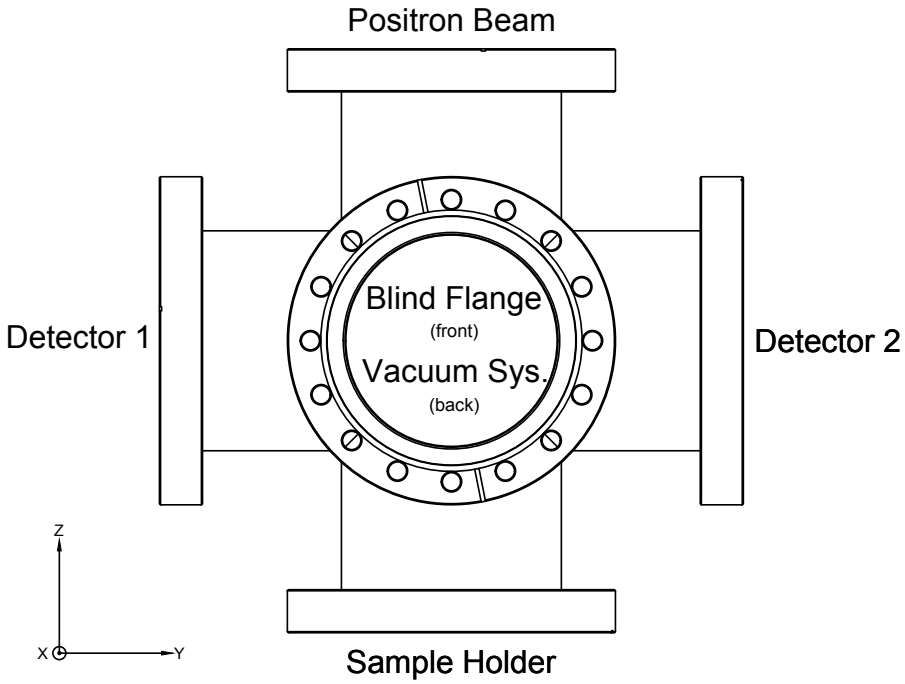

Figure 5.2: Schematic of the six-way crosspiece forming the chassis of the sample chamber.

of the radioactive source, the efficiency of the moderator and the quality of the beam guidance. One way of estimating the particle flux is through the germanium detectors.

By counting the number of detected γ-photons over a given period of time, the rate of annihilations and therefore the flux of positrons can be estimated. Both the geometry of the detectors - i.e. the fraction of the solid angle that they cover - and their detection efficiency have to be taken into account for this calculation. Based on recent measurements and taking all of these factors into account, the total flux can be estimated to be around $3.5 \cdot 10^4$ positrons per second. From measurements performed using the knife-edge method, it is also known that the beam features a diameter of roughly 4.7 mm full width at half maximum (FWHM) at the sample spot at an energy of 10 keV [41]. Combining this information it can be estimated that at the center of the beam the IMX219 (pixel side length = 1.12 µm) will receive a flux of around 0.0025 positrons per pixel per second.

5.2 Sensor Mount Requirements

In order to expose the chosen image sensor to the Lab-Beam, a dedicated mount had to be constructed that replaces the standard sample holder inside of the chamber. This setup

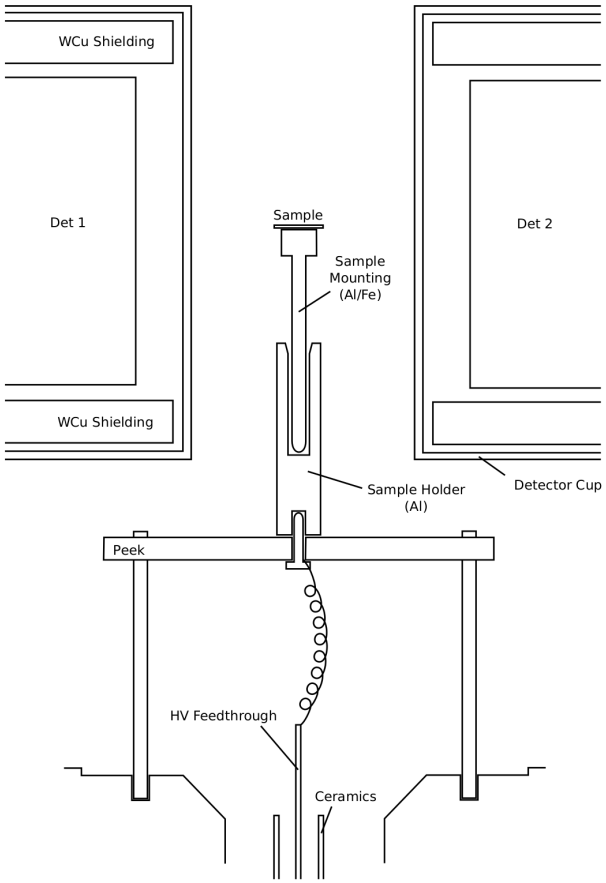

Figure 5.3: Sketch of the standard sample holder used for DBS. Image from [40]

had to house the Raspberry Pi SBC, position the sensor in the center of the beam and meet a range of requirements in terms of electrical, thermal and magnetic properties.

5.2.1 Sensor Positioning

Crucially, the image sensor had to be positioned precisely in the center of the sample chamber in order to receive the maximum positron flux. The active pixel area of the IMX219 is roughly 3 by 4 mm in size which - compared to the beam diameter of 4.7 mm - leaves little tolerance for misalignment. While it is possible to steer the positron beam by adjusting the currents of specific guiding coils, the Lab-Beam will perform best when focused onto the center of the chamber. The positioning of the sensor in the Z-direction (as labeled in Figure 5.2) is somewhat less critical as the horizontal placement. While the germanium detectors are able to acquire the most amount of data when the sample is vertically centered, small deviations in the range of millimeters will not drastically influence their performance. Therefore - due to another set of constraints regarding the

height of the assembly - the sensor is placed 3.5 mm above the detector axis in the final design.

5.2.2 Vacuum Compatibility

While traveling from the radioactive source to the sample, the positrons are prone to annihilate if they interact with any residual gas molecules in their path. It is therefore desirable to achieve the best possible vacuum inside of the beamline and sample chamber. At the very least, the pressure must be low enough so as to provide a mean free path comparable to the length of the beamline. In the case of the Lab-Beam, the positrons have to cover a distance of around three meters from source to sample. If one assumes the remaining molecules to be Nitrogen at room temperature, the pressure necessary to achieve a mean free path of that length is roughly $3 \cdot 10^{-5}$ mbar [42]. Ideally however, the pressure inside of the beamline should be another order of magnitude lower so as to maximize the positron flux.

To accommodate these very low pressures, it is necessary to consider the amount of outgassing caused by the materials introduced into the vacuum chamber. Outgassing describes the process by which dissolved or adsorbed molecules of gas are released from materials exposed to high vacuum. Even the sublimation of certain metals can contribute to this effect. It is therefore vital to consider which construction materials are used when designing a system intended for high vacuum. Plastics are generally to be avoided with the possible exception of Kapton, PEEK or PTFE which are known to exhibit reasonably low rates of outgassing. Also the elements Cd, Zn, Mg, Li, Ba, Pb and Ca are largely incompatible due to their high vapor pressures [43].

To comply with these requirements, copper was used for the main body of the assembly and fasteners made from V4A stainless steel were chosen. However, since the Raspberry Pi SBC and the camera board also had to be housed within the vacuum system, a certain amount of plastics and high vapor pressure metals (in the form of electronic solder) was unavoidable. To minimize their effect, all non relevant components and connectors have been desoldered from the SBC. This included the ethernet port, four USB ports, the GPIO pin header, the HDMI and micro USB port as well as the 3.5 mm audio jack and a 15 pin ZIF display connector. Also the power and status LEDs were removed to avoid light pollution inside of the chamber. The use of a small amount of Kapton foil was necessary to provide both good thermal contact and electrical isolation between two surfaces.

Another measure taken to reduce outgassing was to cut a deep grove along the longitudinal axis of every fastener and thread used in the assembly. Otherwise, the space created at the bottom of blind holes or in between the threads of a fastener and nut could trap gas molecules and release them over extended periods of time.

Finally, every part of the setup was carefully washed in a bath of Isopropanol using an ultrasonic cleaner. This was done in order to remove any surface contaminants that may have been introduced during handling. To test the vacuum compatibility of the setup, the entire assembly was mounted onto a smaller vacuum chamber featuring a residual gas analyser. Using this setup, the composition of the outgassing contaminants and the ultimate vacuum pressure reachable could be measured beforehand. Pumping the test chamber for 24 hours resulted in an ultimate pressure of 10^{-7} mbar and revealed the residual components to be mostly water vapor - most likely originating from the outgassing plastic components of the SBC. These results were well agreeable with the vacuum requirements for the Lab-Beam.

5.2.3 Thermals

Under normal operating conditions, neither the Raspberry Pi SBC nor the camera module require dedicated heatsinks or active cooling. In vacuum however, the waste heat produced by the electronic components can effectively only be dissipated via thermal conduction - any radiative heat losses can be neglected in this case due to the relatively small difference in temperature between the components and their surroundings. Since elevated temperatures have been found to have a detrimental effect on image sensor performance, the thermal characteristics of the experimental setup had to be carefully considered.

The datasheet of the IMX219 specifies an absolute maximum power consumption of 200 mW while the SBC has been measured to draw at most 4 W of power at maximum CPU utilization. In order to dissipate this heat, two main measures were taken. Firstly, the entire casing of the assembly was made from 1.5 mm thick copper sheet. By choosing to manufacture the casing as a sheet metal part, five of the six sides could be formed from one sheet of material - resulting in very good thermal conductivity throughout the assembly. The sensor itself is then directly mounted onto the top surface of the casing - being forced into good thermal contact with the copper by pressing it down using two opposing fasteners. Secondly, the top surface of SBC's CPU is connected to the casing via a dedicated piece of copper sheet - which is mounted to the inside of the assembly

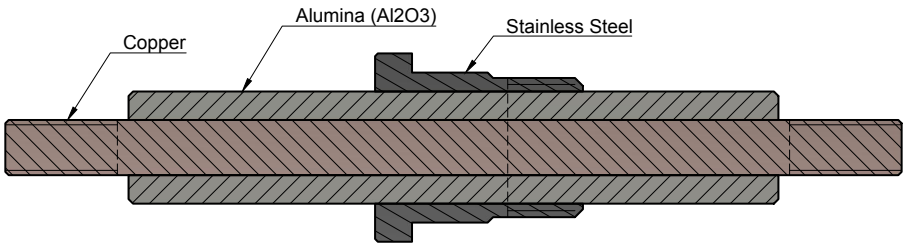

Figure 5.4: Cross section of the high voltage passthroughs used. Not shown is the vacuum compatible O-ring around the stainless steel sleeve.

via a fastener and forced into good thermal contact with the processor by its internal spring force. The heat produced by these two components is thus transferred into the main body of the assembly.

From the copper casing the heat is subsequently transferred into the high voltage passthroughs, whose simplified cross section is shown in Figure 5.4. Their copper core features a large contact area to the electrically insulating sleeve of Alumina which is mounted inside a stainless steel collet. From there the heat is dissipated into the CF 100 flange trough which the passthroughs are mounted. Ultimately the large mass of the sample chamber onto which this flange is installed will serve as the heatsink.

To validate this design, a simple thermal simulation using Autodesk Fusion 360 has been performed. The sensor and the CPU have been set as constant power heat sources and the temperature of the flange contact area was fixed at 25 °C. Most of the fasteners, the SBC itself and the front plate have been removed in this simulation as their contribution to the thermal situation can be neglected. A visualisation of the results can be see in Figure 5.5. The calculated sensor temperature at equilibrium reaches 32 °C while the CPU's temperature raises to almost 57 °C.

Due to multiple assumptions and idealized conditions, these results are most likely too optimistic. For once, the simulation assumes a generic thermal conductivity between contacting surfaces that in reality might be negatively influenced by surface contamination or deformation. Also, two O-rings between the passthroughs and the CF 100 flange have been omitted in this simulation, whose presence will most definitely increase the thermal resistance between those parts. On the other hand, the simulation assumes the maximum thermal output for both the sensor and the SBC. In reality, the CPU will have idle periods in between acquisitions where the data is transferred out or a long exposure is being taken.

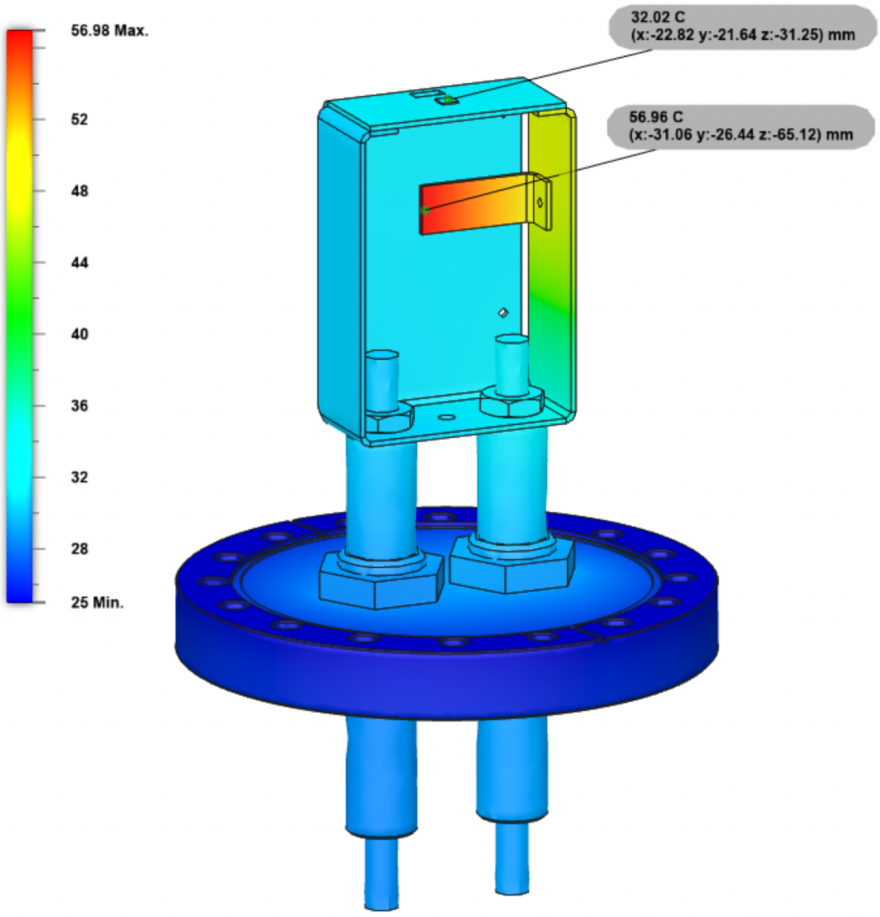

Figure 5.5: Thermal simulation of the assembly conducted using Fusion 360. Some components that do not contribute to the thermals have been omitted.

During the actual experiment, both the sensor and CPU temperature have been recorded and were observed to stabilize at 45 °C and 70 °C respectively during continuous operation, placing them both well within their acceptable operational limits.

5.2.4 Magnetic Requirements

As outlined in section 2.2.1, the preferred method of guiding low energy positrons towards their intended target is to utilize axial magnetic fields. In such a configuration, the positrons spiral around the field lines as a result of the Lorentz force. This method of beam guidance is also used at the Lab-Beam and is realized through solenoid coils wound around the outside of the beamline. In order to guide the field lines produced by these coils towards the material of interest, the standard sample holder used within the Lab-Beam consists of a ferromagnetic rod on top of which the sample is mounted. The

rod concentrates the magnetic field and therefore effectively focuses the positron beam further by reducing the gyration radius of the spiraling particles [40].

As it is desirable to exploit this focusing effect to increase the density of the positron flux impinging on the CMOS sensor being tested, the magnetic properties of the sensor mount have to be considered. To replicate the effect of the ferromagnetic beam guide in the standard sample holder, a 5 mm rod made from St37 low carbon steel is placed within the assembly directly in line with the image sensor. Although copper is weakly diamagnetic, the effects from the 1.5 mm thick layer between the sensor and the beam guiding rod are expected to be negligible. Similarly, the high voltage passthroughs and the rest of the casing will not greatly influence the beam's magnetic guidance. The rest of the fasteners are made from V4A stainless steel which - being austenitic in structure - is essentially non-magnetic and therefore also unproblematic.

5.2.5 High Voltage

In order to accelerate the positrons to the desired implantation energy, a voltage bias is applied between the moderator and the sample. As the entire chassis of the Lab-Beam is grounded, this effectively means that the voltage difference is applied between the sample and the walls of the chamber. The standard sample holder is able to withstand being polarized up to 50 kV, although the typical DBS implantation energies range between 0 and 30 kV. The design requirement for the camera mount was chosen to be 10 kV.

This was realized by using two high voltage passthroughs with a maximum rating of 15 kV. They consist of a copper terminal that is embedded in a sleeve of Alumina - a highly insulating ceramic. (Figure 5.4) Their outer stainless steel collet features a shoulder with an O-ring and a large size nut with which the passthrough can be installed into a 27 mm bore. Two such holes where drilled into a CF 100 blind flange to accommodate the passthroughs.

Another consideration with regards to the acceleration potential was the geometry of the camera mount. To reduce the chance of electrical arcing between the camera holder and the chamber walls, sharp edges and protrusions were to be avoided whenever possible. The rounded corners of the casing - which come courtesy of the sheet metal construction technique - already suited this requirement well. Additionally, any fasteners along the outside of the assembly have been sunk into the material, allowing them to sit flush

with the exterior surface. The remaining sharp edges have been rounded off wherever possible.

Avoiding protrusions was also relevant in the context of beam guidance. Since the negative voltage applied to the casing electrostatically attracts the positrons, any large asymmetries or surface deviations will deflect the beam to some extent. At smaller scales and closer to the target this effect is somewhat less problematic since the positrons' inertia will keep them from deviating too far. In the final design, two round headed fasteners where placed on either side of the image sensor which protruded slightly above the copper surface. While this most definitely altered the electric field close to the sensor, no adverse effects where observed during the experiments.

The possibility of electrical arcing to the chamber walls was of great concern since any sufficiently large discharge would most likely irreversibly damage the SBC inside of the assembly. Therefore, large safety margins where included in every relevant design choice. While the maximum specified voltage of 10 kV was never exceeded during the experiments, a destructive device test was performed at the very end of the measurement campaign in which the bias voltage was increased above the 10 kV limit. It was found that the system was able to operate up to a voltage of 27 kV before an electric discharge inside of the chamber permanently disabled the SBC.

5.2.6 Power Supply

During normal operation the Raspberry Pi SBC requires a stable 5 V power supply capable of delivering at least 5 W of continuous electrical power. Providing this power source presented an unusual challenge since the entire assembly also needs to be kept at a high voltage relative to ground. Therefore, a system had to be developed that would be able to transfer up to 5 W of power while at the same time providing electrical isolation able to withstand up to 10 kV. To that end, a range of different possibilities were considered.

An innovative approach to powering electronics inside of the sample chamber that was successfully tested at the Lab-beam was to use a high intensity LED shining through the glass viewport to power a solar cell within the setup [44]. This method was however clearly unsuitable for the planned experiment due to the intense light pollution caused by the LED and the limited amount of power that can be transferred this way. Wireless power transfer using high frequency electromagnetic fields is also not feasible due to their influence on the beam guidance. Approaches in which the above mentioned

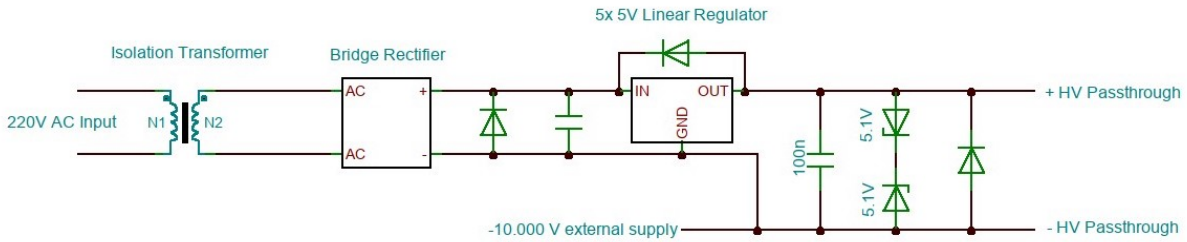

Figure 5.6: Schematic of the isolated 5 V *power supply used to provide electrical power to the experimental setup. On top of the standard functional elements required to produce a stabilized* 5 V *rail the circuit features a number of additional protections designed to absorb occasional high voltage spikes on its outputs. The feature is designed to reduce the probability of damage to the SBC in case of sparking.*

methods of delivery would be pulsed and their energy stored in capacitors or batteries inside of the assembly were also discarded due to the relatively high continuous power required.

The solution that was finally implemented consisted of using two high voltage passthroughs that would both be kept at the required high voltage bias and who would provide the necessary 5 V potential across them. In effect, one passtrough would provide 10 000 V relative to ground, the other one 10 005 V. In order to produce a stable 5 V supply which would be isolated from ground, the circuit shown in Figure 5.6 was designed and build. A custom isolation transformer featuring a secondary coil wound around a spacer machined from PTFE provides an alternating current at around 7 V RMS. This voltage is then rectified and smoothed out before being fed into 5 linear voltage regulators connected in parallel (not shown in schematic). The stable and precisely regulated output is then connected to the terminals of the two high voltage passthroughs. This circuit includes multiple safety features aimed at protecting the SBC in the event of a high voltage discharge; they include two high current diodes for reverse voltage protection, two Zener diodes that clamp the output of the linear regulators to a maximum of 5.1 V and a ceramic capacitor to protect against fast voltage transients. The high voltage bias is provided by a dedicated power supply and is injected into the negative rail of this circuit.

The isolation transformer was built by replacing the secondary coil of an existing power transformer with a specially made PTFE spacer that guarantees a minimum of 5 mm of material between the secondary windings and the transformer core. Depending on the exact composition, PTFE features a breakdown voltage of up to 20 kV/mm - allowing this design to facilitate a theoretical maximum voltage of 100 kV [45]. A cross sectional

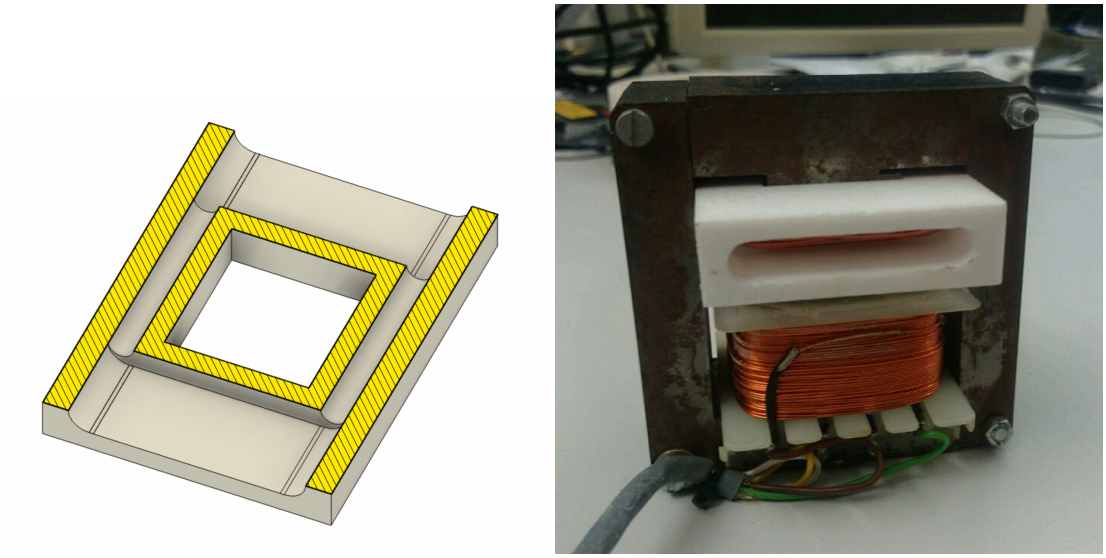

Figure 5.7: Cross section view of the PTFE spacer (left) and image of the isolation transformer (right).

view of the spacer and a picture of the finished isolation transformer are shown in Figure 5.7.

Since the entire 5 V power supply would be placed outside of the vacuum system and held at a high voltage, special care had to be taken to ensure operational safety around the experimental setup. To that end, the circuit was housed inside a section of aluminum pipe which in turn would be mounted directly onto the high voltage passthroughs. A shield made from acrylic tubing was constructed which could be clamped around the CF 100 flange and would prevent direct access to the exposed metal surfaces. The transformer was placed on the ground beneath the sample chamber and connected to the isolated power supply via two thick cables. Large diameter conductors were desirable in this case in order to reduce any corona discharge caused by the high voltage potential. Figure 5.8 shows the complete setup installed beneath the sample chamber of the Lab-Beam.

5.2.7 Communication

The entire experiment would be controlled by the same PC that manages the operation of the Lab-Beam. This machine controls all relevant aspects of the positron beam and allows for automated measurements and data acquisition. In order to receive instructions and transfer the acquired frames, the Raspberry Pi SBC needed to have a reasonably high-

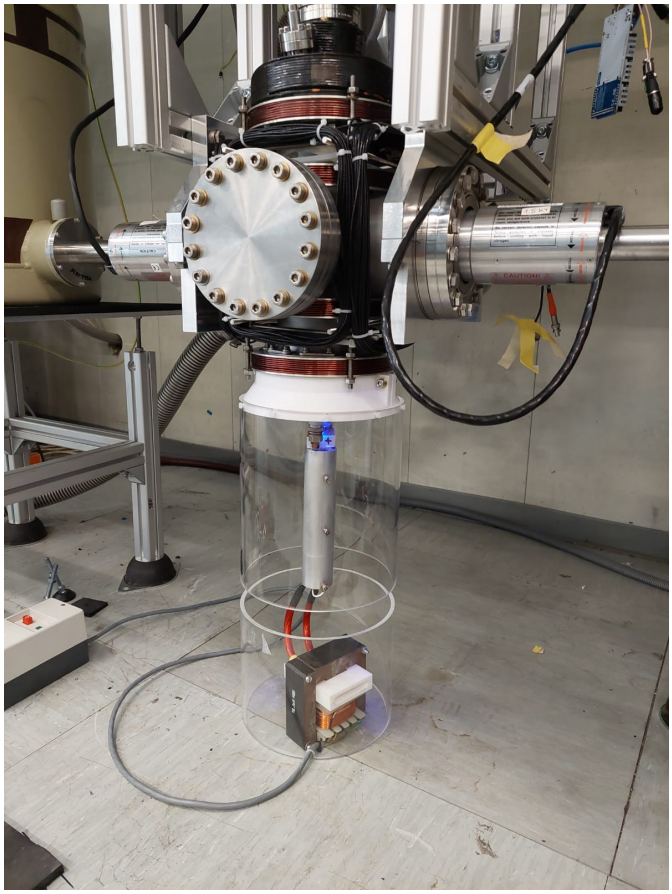

Figure 5.8: The isolation transformer and the 5 V *power supply mounted to the underside of the sample chamber. Not shown in the photo, the high voltage cable providing the acceleration potential used to set the positron implantation energy.*

bandwidth connection to the control computer. Even using the packed pixel format, each frame of the IMX219 requires around 10 MB of bandwidth.

Any kind of optical communication would generate light pollution and was therefore unsuitable. Wired connections were also infeasible due to the required high voltage isolation. The most convenient approach was the use of wireless communication in the form of 2.4 GHz WiFi. This was initially thought to require special modification to the setup as the sample chamber was expected to act as a Faraday cage and block any wireless signal coming from within. Additionally, the copper casing of the camera mount itself represents an enclosed metal space that would further attenuate any signal.

However, tests within a smaller vacuum chamber of similar construction revealed that the SBC was perfectly able to establish connection to a WiFi transmitter placed outside of the chamber and data rates of up to 3 MB/s were easily achieved. Since the SBC features a built in WiFi antenna, no further modifications were necessary. In the final

setup, a WiFi antenna was placed directly outside of the sample chamber and connected to the control computer via USB. This yielded a stable and reasonably fast connection to the experimental setup.

5.3 Sensor Preparation

To perform the planned experiment, the image sensor first had to be stripped of its color filter and subsequently coated with a thin layer of phosphor. The chosen type of phosphor - a compound consisting of silver doped zinc sulfide which has been shown to exhibit positron induced luminescence - had to be evenly applied in a thin layer across the pixel area. In 2018, Stenson et al used a 50-70 µm thick layer of this type of phosphor to investigate its interaction with positrons [9].

To reliably deposit layers of comparable thickness onto the sensor, the phosphor was first suspended in a solution of ethanol and then carefully dispensed onto the sensor's surface. The ethanol was then left to evaporate, leaving a uniform coating of phosphor behind. By precisely controlling the amount of suspension used, the thickness of the resulting layer could be varied.

The layer thickness was verified using a computer based light microscope. This could be done by bringing part of the sensor's edge into view, so that both the phosphor coating and the surface of the Silicon dye were visible. By focusing the microscope first onto the Silicon dye and then onto the top most particles of phosphor, the difference in height could be gathered from the positions of the microscope's motorized stage. While this method relies on visually finding the best focal distance at each step, the accuracy is estimated to be on the order of $\pm 10\,\mu m$.

Using the method outlined in Section 4.4.2 the color filter of the sensor was removed and a 70 µm thick layer of phosphor subsequently applied.

5.4 Additional Considerations

In order to distinguish any signal caused by positrons from possible other sources like light pollution or noise, a thin wire with a thickness of 125 µm was installed directly in front of the image sensor. If the positron beam would indeed form an image on the sensor, its behaviour would be comparable to that of a collimated light source and the

wire would form a well defined shadow across the frame. We can expect any stray light that might be present inside of the sample chamber to be strongly reflected by the camber walls and therefore constitute a very diffuse source of light. A signal generated by stray light would therefore not produce a sharp shadow.

The two fasteners that mount the image sensor onto the casing were used to clamp the filament in place, positioning it roughly 0.5 mm above the pixel array. In Figure 5.10 the wire and the method with which it is mounted can be seen.

Amongst other types of sensors, the vacuum system of the Lab-Beam uses multiple Pirani gauges in order to monitor the very low pressures inside of the beamline. A Pirani gauge consists of an electrically heated wire that is exposed to the vacuum. Since the amount of heat loss is proportional to the number of molecules colliding with the wire, this setup can be used to measure the vacuum pressure by carefully monitoring the amount of current necessary to keep the wire at temperature. Usually the wires are heated to the extent that they emit visible light via black body radiation. As this light would subsequently also find its way into the sample chamber and interfere with the measurement, the vacuum gauges had to be switched off prior to image acquisition.

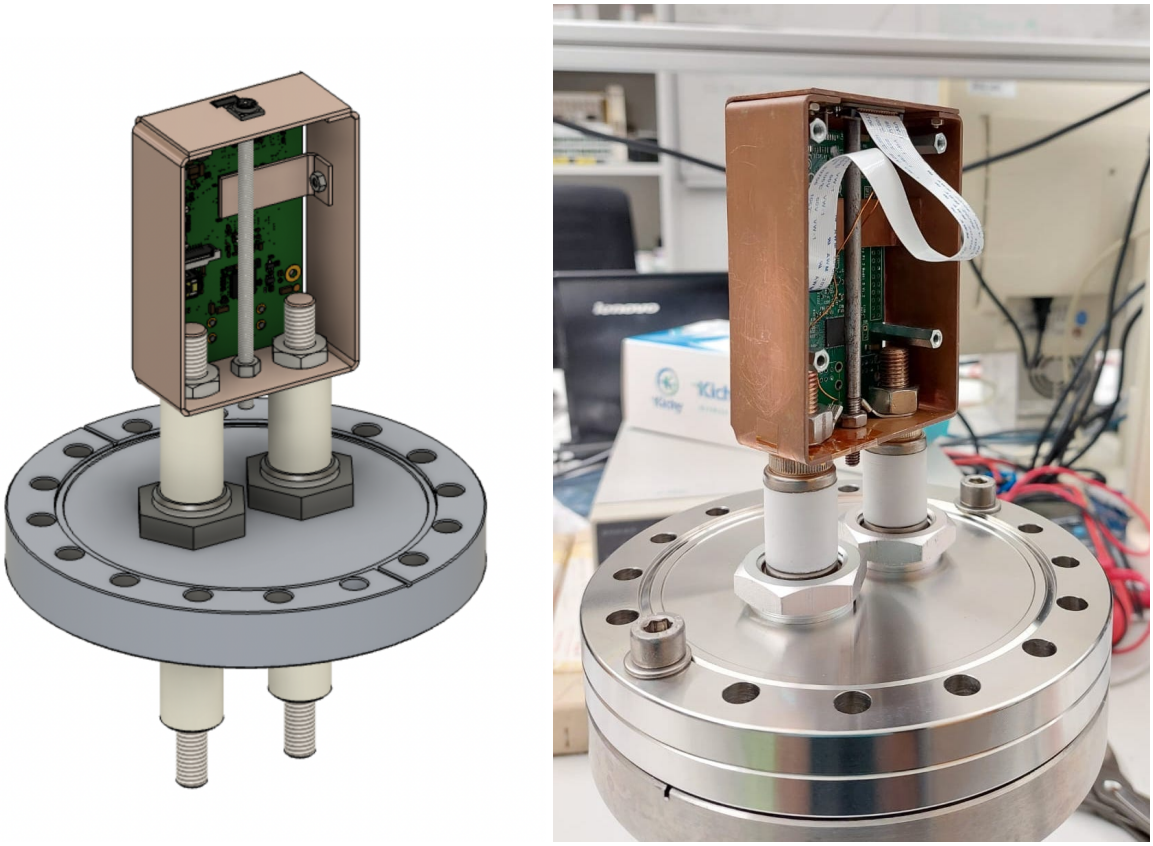

Figure 5.9: A CAD model of the final camera mount design (left) and an image of the assembly (right). The green circuit board is a Raspberry Pi SBC while the board connected via the white flex cable houses the IMX219 camera. Both representations are missing the front panel.

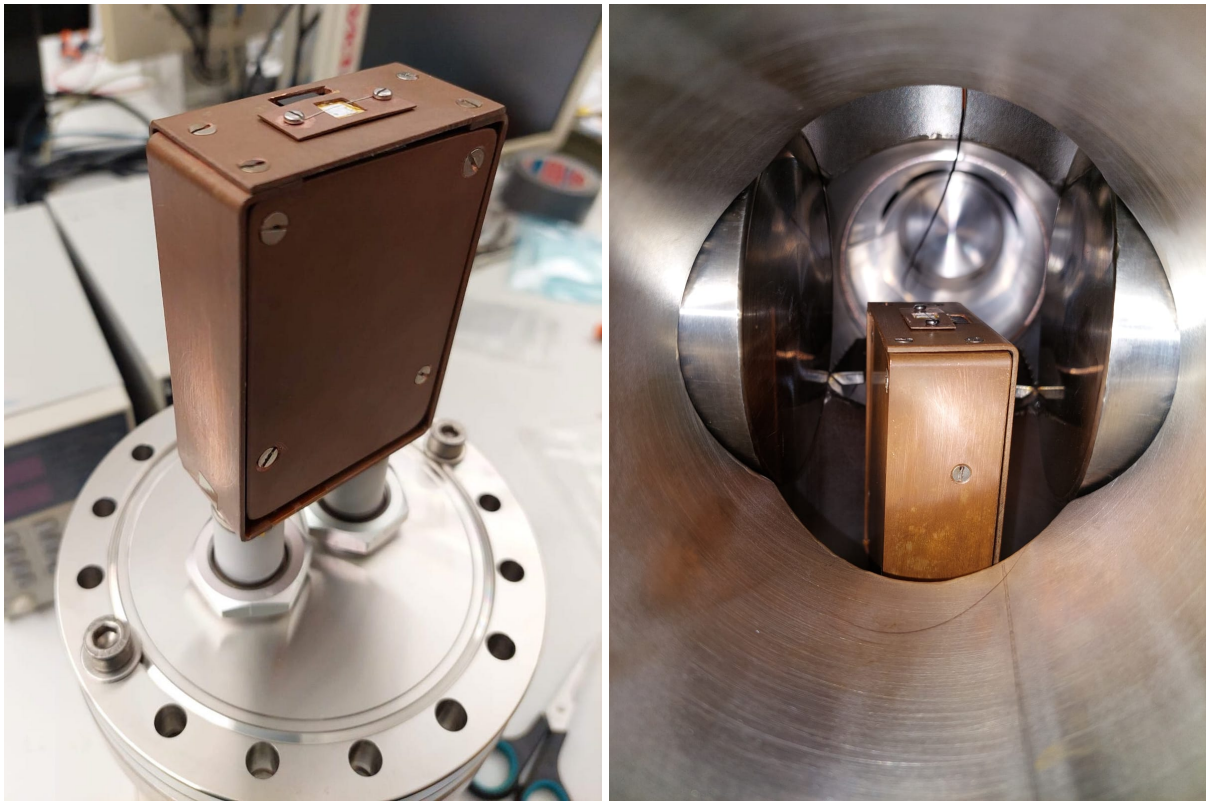

Figure 5.10: An image of the camera mount with its front panel mounted and image sensor installed (left); and an image of the assembly mounted inside of the sample chamber (right). Due to a design constraint of the Lab-Beam, the assembly is mounted at a slight angle relative to the detectors.

6 Experimental Results and Discussion

6.1 Phosphor Coated Sensor

The first experiment was conducted using an image sensor with its color filter removed and a 70 µm thick layer of EJ-600 ZnS:Ag phosphor applied to it. The positron energy was initially set to 10 keV since this was expected to yield the strongest signal. The image sensor was configured for an amplification factor of 85 and an exposure time of 31 seconds. Using these parameters, the series of images shown in figure 6.1 was produced.

A well defined shadow caused by the wire in front of the sensor can be see across all images, providing strong evidence that the signal is in fact caused by the beam of low energy positrons. By varying the current passing through the vertical correction coil "C4V" - which is placed around the 90° bend in the beamline - the beam can be effectively steered across the image, further validating the assumption that the signal is produced by the positron beam. The two distinct dark areas that can be seen across all images are most likely caused by inhomogeneities in the phosphor coating.

By fine tuning the sensor parameters, it was possible to increase the amplification factor to a value of 128 and reduce the exposure time to 11 seconds while still being able to clearly distinguish the beam shape.

6.1.1 Beam Shape and Position

In order to characterize the influence of the correction coils on beam position, the beam was repeatedly scanned across the image sensor and the corresponding coil currents recorded. This experiment was aimed at determining how linear the relationship between coil currents and beam defection would be. Previous analysis of the Lab-Beam indicate that the beam response to the correction fields is highly non-linear due to the complex nature of the magnetic guidance system [46].

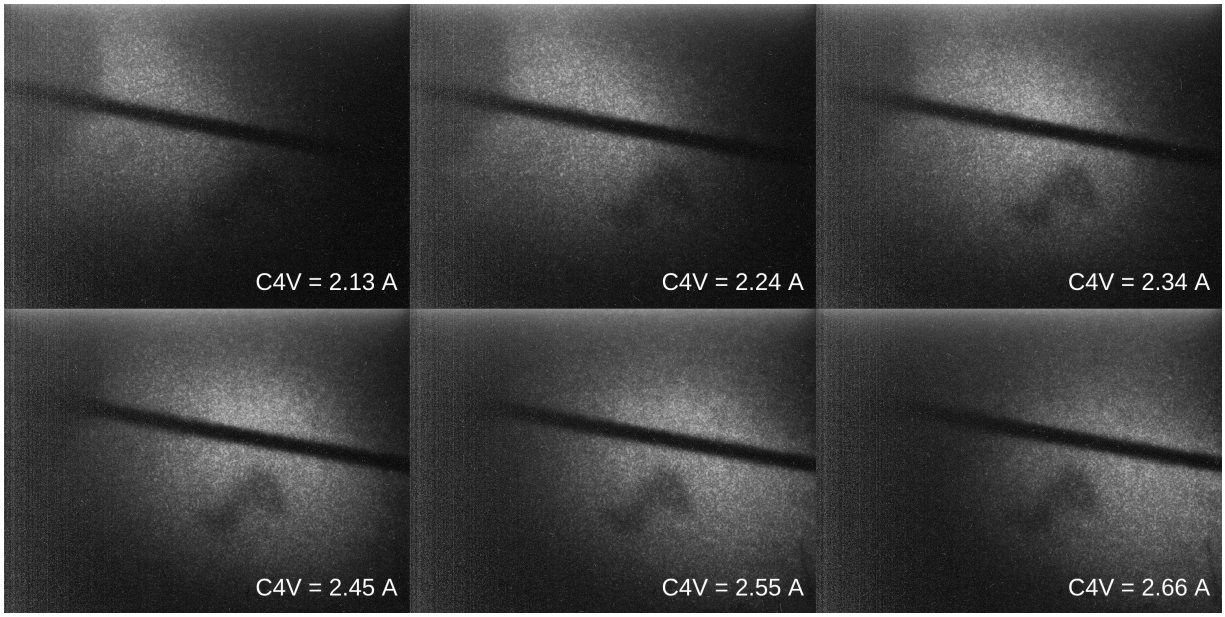

Figure 6.1: A series of images produced by implanting positrons with an acceleration potential of 10 keV*, an analog amplification factor of 85 and 31 seconds of exposure. The current through the vertical correction coil "C4V" was varied across the images, resulting in the deflection of the beam center. The dark band across the picture is the shadow of a* 125 µm *thick metal wire installed in front of the sensor; the darker regions in the top-left corner and close to the center of the sensitive areas are caused by inhomogeneities in the phosphor coating applied onto the sensor.*

The average brightness over the entire frame was employed as a proxy indicator of the centering of the beam with respect to the sensor. While a more accurate method for determining the beam position will be introduced later, this rather simple approach proved sufficient for the purposes of this measurement. Figure 6.2 shows a plot of the signal intensity over the sensor as a function of the correction coil current. A maximum in intensity is present in the plot con correspondence of a 0 A current in coil C4H and 2.6 A in coil C4V; the intensity then monotonically decreases as the deflection imposed to the beam increases, pushing it further away from the sensor area. This technique could already be used, without further refining, to completely automate the beam centering in an apparatus similar to the Lab-Beam.

An alternative way of interpreting the plot in figure 6.2, is as a way of using the positron beam to indirectly image the shape of the CMOS detector. In fact, by representing the mean brightness values on a colored scale and plotting them over a 2D array of current values, a (very low resolution) image of the sensor's active pixel area is formed. Such an image would be distorted by the non-orthogonality and nonlinearity of the positron beam deflection in the current applied to the coils; still the rectangular shape of the

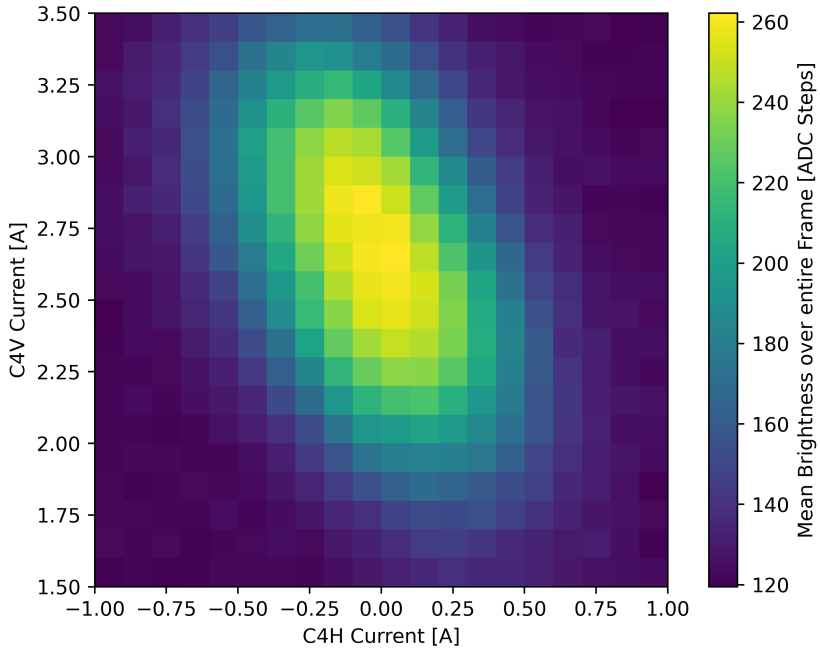

Figure 6.2: Average brightness over the entire frame versus the correction coil currents. The coils being adjusted are the horizontal (C4H) and vertical (C4V) correction coils. A global maximum can be observed where the beam is centered onto the sensor.

sensor and its slight angle with respect to the Lab-Beam major axis is clearly visible in figure 6.2.

This result confirms that, within the size of the CMOS sensor, the beam deflection does respond to the deflection current in a rather linear fashion. However, it has to be noted that at roughly 3 by 4 mm, the sensitive area of the sensor is relatively small compared to the samples commonly analyzed at the Lab-Beam. It would not be unrealistic for the deflection to become increasingly non-linear across greater distances.

Another major aspect which influences the beam shape and position is the acceleration potential. At higher energies the beam inherently becomes more focused and is drawn towards the target. As a consequence, the correction currents have to be adjusted when lowering the positron energy in order to keep the beam centered onto the sensor. An increase in the beam diameter as the acceleration potential decreases is clearly visible in the images recorded by the CMOS sensor: figure 6.3 shows a series of images acquired at varying positron energies. Crucially, the exposure time and amplification factor also need to be increased with decreasing beam energy so as to compensate for the reduction in brightness; even taking this into account, the beam spot can still be observed to

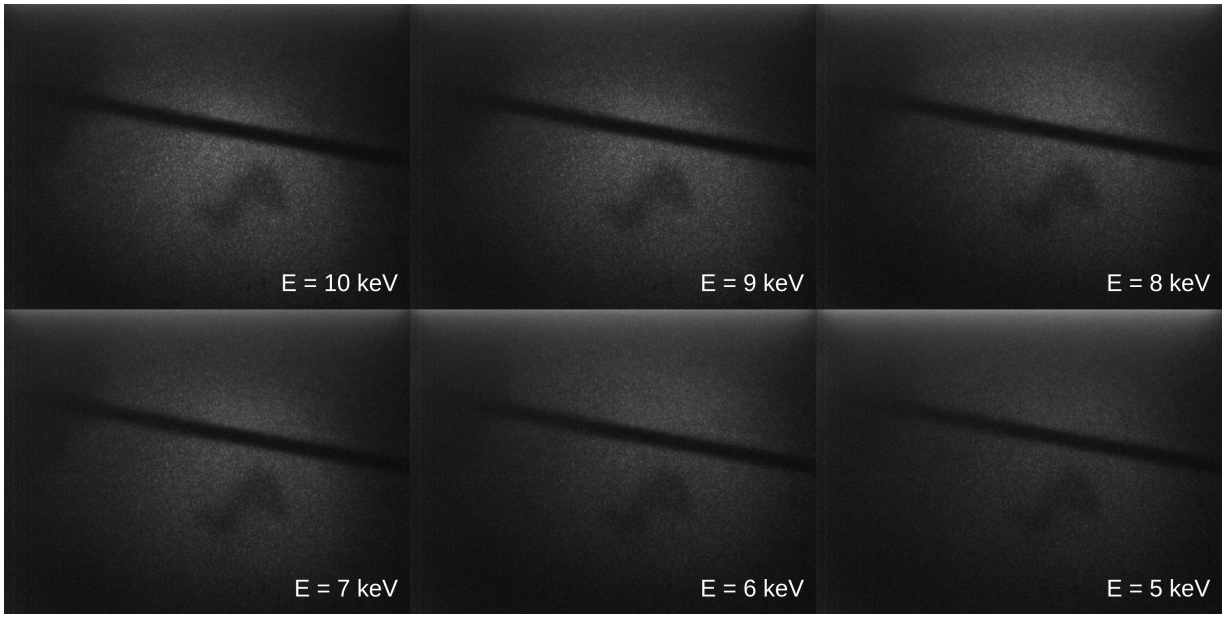

Figure 6.3: Imaging of the positron mean with varying kinetic energies. Clearly visible from the sequence is the increasing spot size as the acceleration potential is decreased. Not visible is the dimming caused by the decreasing positron flux and phosphor excitation as the exposure time and analog amplification factor have been varied so as to keep the signal strength constant.

become dimmer at lower energies due to its increasing size and consequently decreasing positron flux.

To keep the beam centered at lower energies, the correction currents had to be continuously adjusted. To automate this process, a program was written that would decrease the acceleration potential in small increments and iteratively adjusts the coil currents at each step so as to maximize the image brightness - therefore centering the beam again. The best coil settings for each energy were recorded and a least-squares linear fit calculated. The results are plotted in figure 6.4. On top of constituting a valuable reference for the future operation of the Lab-beam, these results then provided optimal values for the correction currents to be used in subsequent measurements at varying energies - see e.g. figure 6.3.

To test how the necessary correction currents change with target geometry, the entire camera assembly was rotated by 180° inside of the sample chamber and the centering optimization repeated. Since the casing of the camera assembly is largely symmetrical, the required correction currents were expected to remain largely unchanged. However, the results obtained from this follow-up experiment showed an entirely different trend and large discrepancies in the necessary currents. This leads to the conclusion that

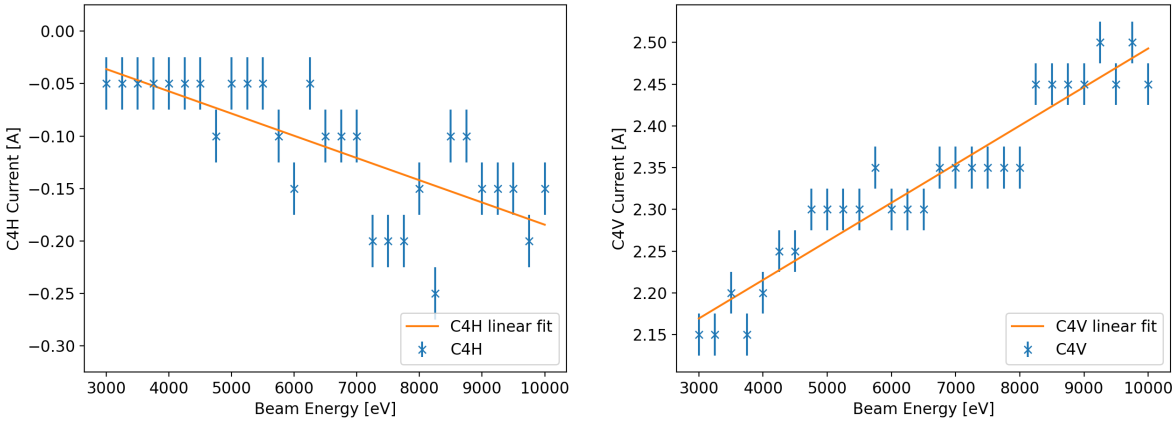

Figure 6.4: The correction coil currents necessary to keep the beam centered at varying energies as determined using the total signal intensity in the CMOS sensor as a metric for the beam centering. The discretization in the vertical axis stems from the optimization algorithm employed (maximization over a fixed grid scan).

even slight changes in the target geometry can have a strong influence on the beam electrostatic and magnetic guidance. In this specific case it is suspected that the large differences in beam deflection between the two configurations are caused by asymmetries in the electric field close to the target.

While the average brightness over the entire frame was an adequate metric for beam centering, a more precise and comprehensive method of extracting information on the beam shape was desirable. To that end, Dr. Guatieri developed a program that is able to fit a 2D Gaussian function of the beam cross section onto the images. The software is "trained" by providing many images with the beam in different locations and sizes across the frame. The training process has the goal of computing what we have named the *fit context*; the *fit context* describes obstructions and differences in sensitivity across the frame so that the fit algorithm can take them into account. An accurate fitting context will - for example - take the shadow of the wire, the denser areas of the phosphor and static image noise into account. Once successfully trained, the software can be used to determine the parameters of the best fitting 2D Gaussian curve from the images - including the center, the size, the orientation and the amplitude. This capability was crucial to the analysis and evaluation of the subsequent measurements.

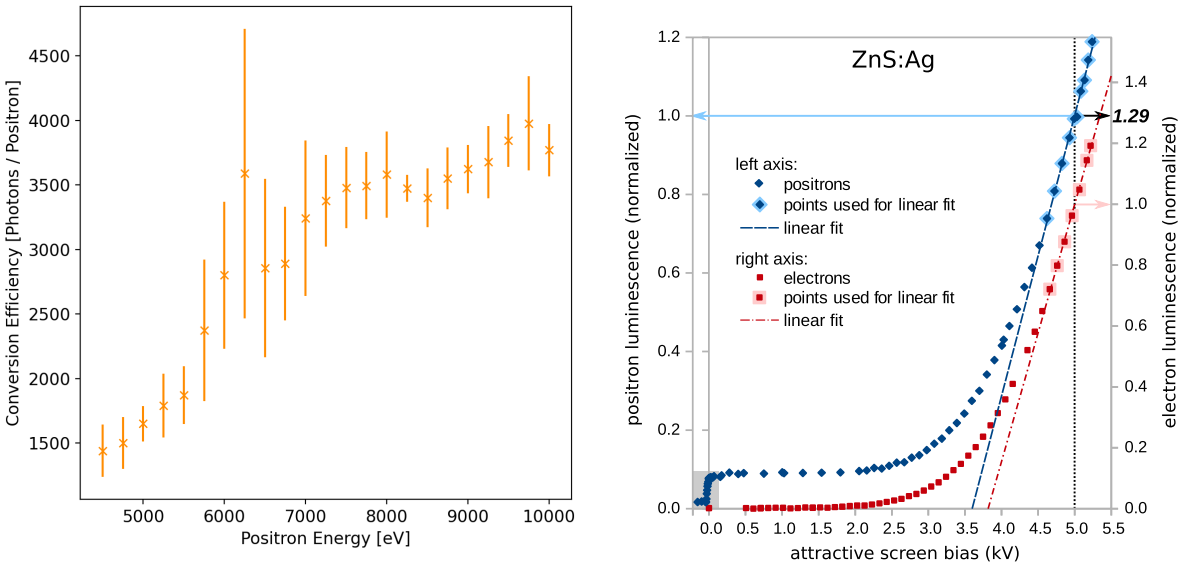

Figure 6.5: Phosphor conversion efficiency in our apparatus as a function of the positron kinetic energy (left) and relative phosphor luminescence as measured by Stenson et al (right, image from [9]).

6.1.2 Phosphor Efficiency

An important and previously unknown characteristic of the EJ-600 ZnS:Ag phosphor is its positron conversion efficiency. While Stenson et al were previously able to characterize the phosphor's relative induced luminescence at different positron energies, no absolute values for the ratio of photons produced to positrons implanted were available.

To compute the conversion efficiency from the acquired images, the amplitude of the 2D Gaussian fit was compared to the positron flux calculated in section 5.1. This was done at various energies ranging from 4.5 to 10 keV. The results are plotted in figure 6.5.

The resulting values indicate a conversion efficiency of roughly 3800 ± 600 photons/positron at an implantation energy of 10 keV. However, these results are troublesome at best when considering the energies involved. The emission spectrum of the phosphor is centered around 450 nm – corresponding to a photon energy of 2.75 eV. A positron at 10 keV therefore only possesses enough kinetic energy to produce at most $\frac{10000}{2.75} \simeq 3600$ photons at this wavelength. While this value by itself would be within the measurement error bar, the image sensor only covers half of the solid angle making the theoretical maximum efficiency 1800 photons/positron. Furthermore, intrinsic inefficiency, self absorption and other loss mechanisms within the

phosphor are expected to impact the phosphor efficiency, which further detract from the realisticity of the measurement result. However, the positron kinetic energy is not the only source of energy which can produce light emission within the phosphor.

Firstly, positrons are expected to cause additional excitation in the phosphor via Auger-mechanisms and secondary γ-photons. The measurements by Stenson et al indicate that these effects only account for around 10% of the total emission at a positron energy of 5 keV and that their contribution does not scale with implantation energy; therefore, while present, this effect cannot by itself explain the discrepancy.

Another phenomenon that needs to be taken into account when interpreting the apparent phosphor conversion efficiency is the direct influence of positrons and of their secondary particles on the image sensor. We can easily exclude any mechanism by which positrons directly enter the sensor to generate a signal since the 70 µm thick layer of phosphor is virtually impenetrable to 10 keV positrons and consequently to secondary electrons produced by their stopping. Secondary electrons produced by high-energy Compton scattering of the γs produced by the positron annihilation, however, do have enough range to reach the CMOS sensitive area. In fact, as we will discuss later in section 6.3, frames acquired using an unmodified sensor exposed to the beam have been observed to feature numerous white streaks that are likely caused by these secondaries. While these artifacts do contribute to increase the signal registered by a sensor covered in phosphor, the density with which we have observed them to appear is far too low to account for the large offset in efficiency. Figure 6.12 shows the streaks in an image acquired at similar camera settings without phosphor.

The most plausible explanation, given the data currently available to us is that Auger and gamma induced emissions of the phosphor manifest not only as visible photons around the main emission peak of 450 nm but also as ultraviolet light; as is, coincidentally, the behaviour of undoped ZnS [47]. Ultraviolet light produced by positron annihilation in the phosphor would not be detected in the setup used by Stenson et al as in that case the phosphor screen was imaged through a glass viewport which would filter UV radiation. The IMX219 sensor has been shown to be sensitive to 310 nm light, making it possible for it to register UV emissions from the phosphor [37]. That way, the energy introduced by the Auger mechanism and annihilation gammas would be underestimated in the data produced by Stenson et al and could account for the increased signal observed in our experiments. We find this hypothesis compelling and worthy of further investigation.

The data acquired by Stenson et al also shows that in the region below 2.5 keV the positron induced luminescence is practically constant with respect to the implantation

energy. This finding has further implications about what the lowest detectable positron energy would be in the apparatus being characterized in this thesis. While a weak signal could still be observed at an implantation energy of 3 keV, the beam was no longer detectable at values below that. However, since the conversion efficiency has been shown by Stenson et al to remain largely constant in this region, it is strongly suspected that the lack of signal is caused by the dramatic increase in beam diameter and therefore lower flux rather than by a lack of luminescence. It was therefore concluded, that if the beam had remained well focused at lower energies, it would have most likely been detectable even at near-zero implantation energy.

6.1.3 Spatial Resolution

As one of the most desirable future applications of this detection technique is the characterization of positron microbeams, the maximum spatial resolution was of great interest. In the case of a phosphor layer on top of an image sensor, the limitation is given both by the layer thickness and the phosphor grain size. Since the phosphor will emit its light in every direction upon excitation, light originating from the top of the layer will inevitably bleed into a wider area of the sensor. The minimal resolvable feature size is therefore directly proportional to the layer thickness. The minimal layer thickness is, in turn, limited by the phosphor's grain size. The ZnS:Ag phosphor used in these experiments features a grain size of around 8 µm - however, the layer thickness was chosen to be much larger at 70 µm. Visually, the resolution achievable with this setup was on the order of tens of µm, and so comparable to the layer thickness. (Figure 6.6)

6.2 De-Bayered Sensor

As a follow up experiment, the behavior of the image sensor when exposed directly to the positron beam was also characterized. In this setup, the microlens array and color filter were removed but no additional coating was applied. This configuration would be refereed to as a de-bayered sensor.

6.2.1 Detection Efficiency

When positrons were implanted directly into the imaging sensor, the individual particles could be detected as localized clusters of bright pixels. Figure 6.7 shows a magnified

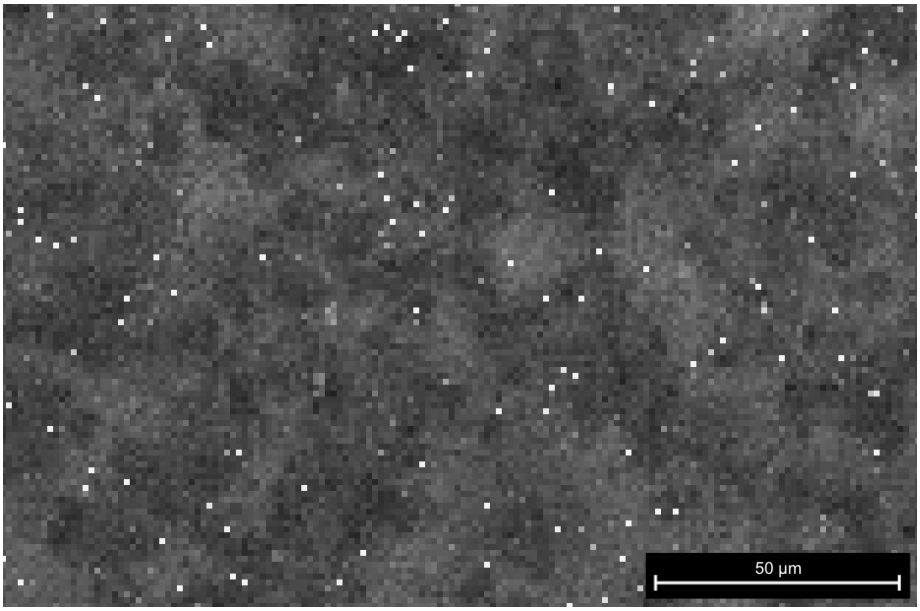

Figure 6.6: A highly magnified view of the area illuminated by the positron beam. Individual grains of the phosphor, 8 µm in size are clearly visible as variations in the brightness recorded by the sensor.

section of an image acquired with this setup. While some detection events manifest as single bright pixels, in most instances the signal generated by the positron bleeds out into adjacent pixels, forming either 1x2 or 2x2 clusters. It is suspected that this pattern occurs when a positron is implanted near the edge of a pixel of in between them. As will be shown later, it might be possible to extract additional information on the precise location of the positron by considering the brightness of these adjacent pixels. It is noteworthy that the sensor amplification factor necessary to produce images where single events could be unambiguously distinguished from the background was found to be comparatively low at roughly 5x. By varying the exposure time, the density of detected events in the image could be tuned. An exposure time of 2.5 s yielded images where most events were separated from each other with little overlap.

By programmatically counting these events and comparing them to the theoretical positron flux, the detection efficiency of this setup can be calculated. Figure 6.8 shows a plot of the resulting detection efficiency as a function of the positron energy. At 10 keV the detection efficiency approaches 100% while below 5.5 keV practically no events are registered. We can, reasonably, interpret this dependency as the positron implantation profile reaching the sensitive portion of the detector as the implantation energy increases. According to Makhov's model this would place the beginning of the sensitive area between 250 and 350 nm from the sensor surface, which is realistic considering the necessity to protect the surface of microchips with a passivation layer of either Silicon

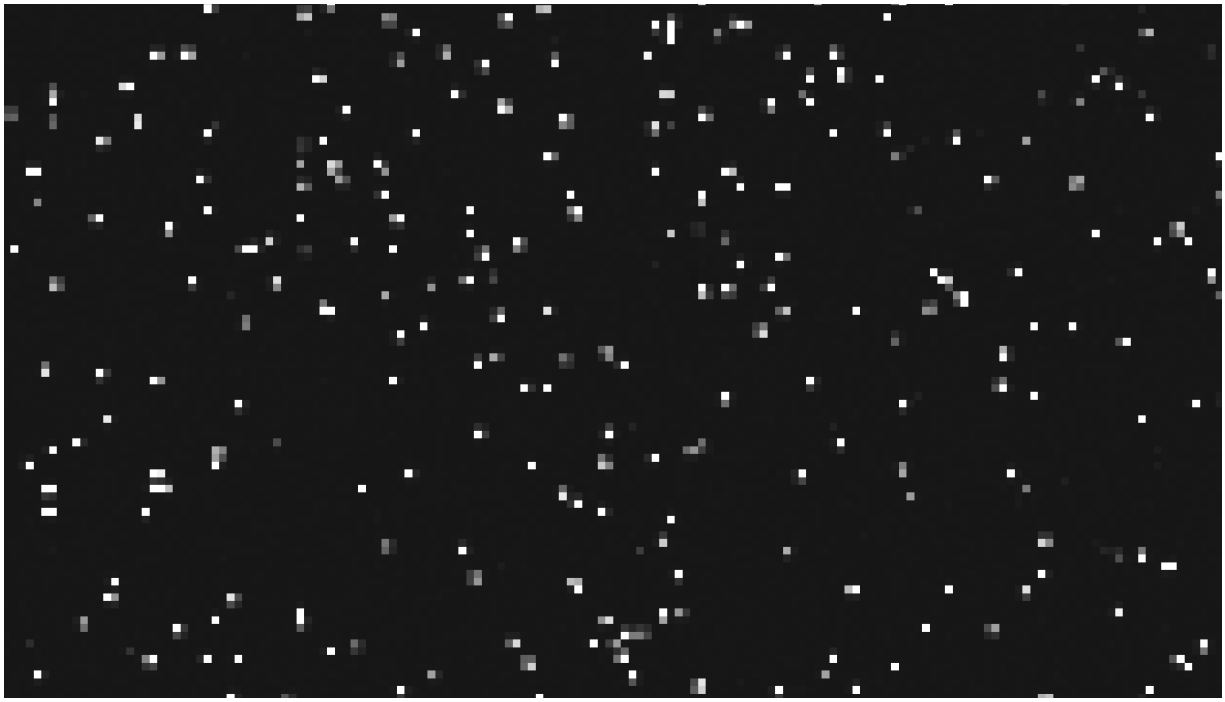

Figure 6.7: Section of an image acquired by a de-bayered sensor. The individual positrons manifest either as single bright pixels or as clusters of 2x2 pixels. This image was acquired with a beam energy of 10 keV*, amplification factor 5.3 and an exposure time of 2.5 seconds.*

nitride or oxide [48]. As we will see, this is consistent with other observations.

6.2.2 Implantation Depth Scan

In addition to the images acquired by the sensor, the germanium detectors built into the sample chamber were employed to characterize the sensor via DBS. Specifically, as the implantation energy was varied during the sensor characterization an implantation depth profile was produced. A DBS implantation depth profile shows the dependency of the parameters used to characterize the shape of the 511 keV peak as a function of the implantation energy; these parameters are commonly named S and W. The S and W parameters are defined as the ratio of the integral of different regions of the γ-energy spectrum; the regions are carefully chosen to make S and W be a measure of the width of the 511 keV peak in the recorded spectrum. The width of the 511 keV peak, and by proxy S and W, can be used to infer different material properties. In our case, the change in the S parameter can be used as an indicator for the transition between different layers in the image sensor. An implantation depth scan of a de-bayered sensor is shown in figure 6.9.

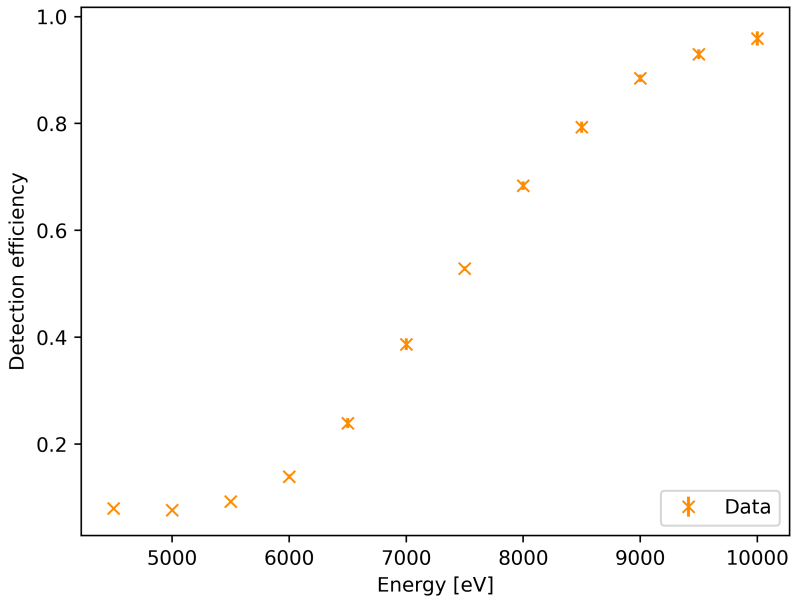

Figure 6.8: Detection efficiency versus positron energy of the de-bayered sensor calculated by counting single detection events and comparing their total number to the expected positron flux. Almost no signal can be detected up to an implantation energy of 5 keV*; as the implantation energy increases, so does the detection efficiency, reaching close to 100% at an implantation energy of* 10 keV*.*

While the absolute values of the S and W parameter are of lesser importance in this case, any relative change in the S parameter indicates a layer transition. The slight increase in the S parameter at very low energies is most likely attributed to surface effects and can be ignored. However, a very definite transition can be observed between 4 and 7 keV. Once again using Makhov's model, this would correspond to a median implantation depth of 200 nm. Combined with the detection efficiency considerations, this would place the transition between the passivation layer and the substrate about 200 nm from the sensor surface and the sensitive portion of the sensor between 50 and 150 nm from the surface of the substrate, which is compatible with the typical scale of modern microelectronic construction processes. [48].

6.2.3 Spatial Resolution

By solely considering single bright pixels - or the brightest pixel in a 2x2 detection event - the spatial resolution of the setup is equal to the pixel size - in this case 1.12 µm. By acquiring images at longer exposure times and summing multiple frames, a very

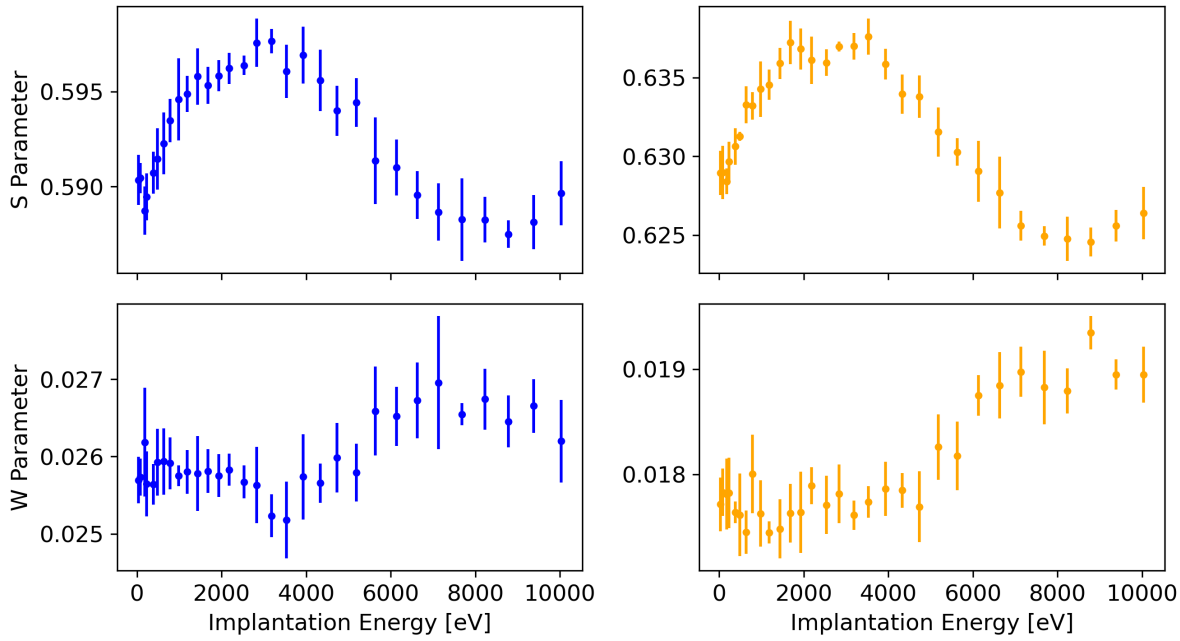

Figure 6.9: Implantation depth scan of a de-bayered sensor produced by Doppler broadening spectroscopy. The color in the plot distinguishes between different detectors – blue representing detector OAA, orange OAB. Below 2 keV *of implantation energy, surface effects are visible as a decrease in value of the S parameter; a transition between materials is visible in the spectrum between 4 and* 7 keV*, once again manifesting in the form of a decrease in the value of the S parameter. To a lesser extend, the transitions are also visible in the W parameter.*

detailed image of a micro feature on top of the sensor can be formed. Figure 6.10 shows such an image depicting the edge of a piece of aluminum foil which has been placed onto the pixel array.

Based on the assumption that a detection event manifesting as 2x2 pixels with varying brightness is caused by a single positron being implanted close to the edge or in between pixels, the position of the event can in fact be inferred with sub-pixel accuracy. In effect, each pixel can be divided into 9 sub-pixels and the position of the detected positron assigned by weighing the brightness values of adjacent pixels. Dr. Guatieri implemented this approach in software and was able to generate upscaled images by providing many detection events and summing the resulting positional information in one frame. While this method still requires fine tuning and a more detailed evaluation, the initial results seem promising. Figure 6.11 shows an upscaled image of the same piece of aluminum foil - this time with a pixel size of 370 nm.

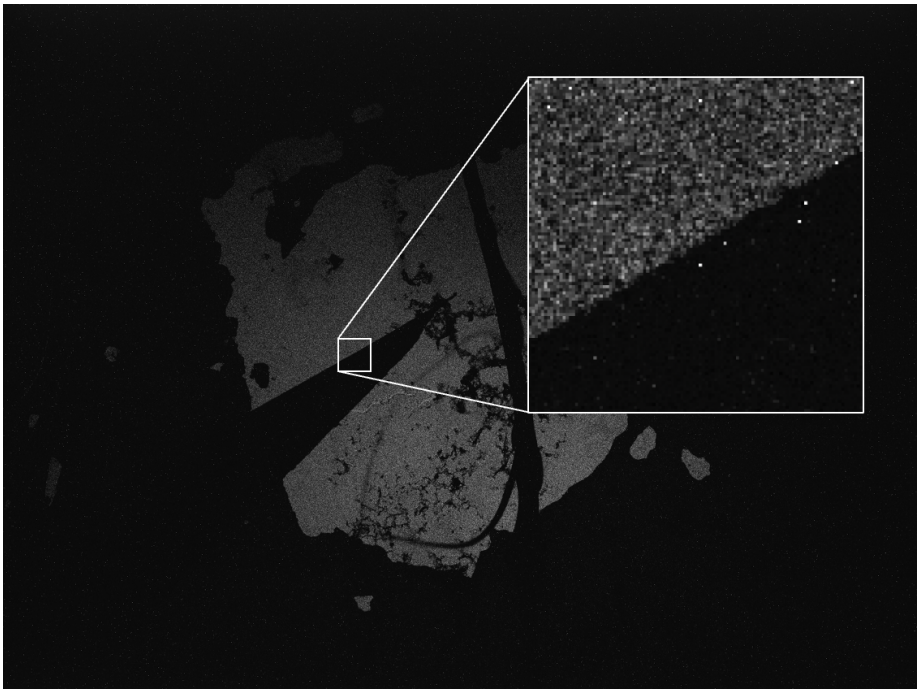

Figure 6.10: Imaging of a millimeter-long wedge of aluminum foil ($\approx$ 10 µm in thickness) deposited onto the imaging sensor produced by the detection of a positron beam aimed at the sensor. The incident positrons were accelerated to an energy of 10 keV*; not enough for them to reach through the thickness of the foil, which makes it appear black in the picture. The color filter has only been partially removed from the sensor, resulting in an irregularly shaped sensitive area. The image was produced by summing 150 frames each acquired at an exposure time of* 2.6 s*. In the inset the edge of a microfeature is shown, the blurring spanning about two pixels in the direction orthogonal to the transition. This is compatible with the blurring induced by the distance between the foil and the sensor surface.*

6.2.4 Sample Rate

While the relatively low particle flux of the Lab-Beam usually required relatively long exposure time on the order of seconds, the IMX219 is also capable of capturing extremely short exposures. By setting the relevant sensor registers is was possible to achieve exposure times of 28 µs. When capturing the beam for such brief intervals, one can expect to image around one positron every ten frames. This prediction matches well with the observations made when acquiring a series of such ultra short frames. In these test it was usual to observe one - or at most two positrons in a single frame while the majority of images remained dark.

It should however be noted that it is not possible to continuously acquired frames every 28 µs due to bandwidth limitations. The time between ultra short exposures is

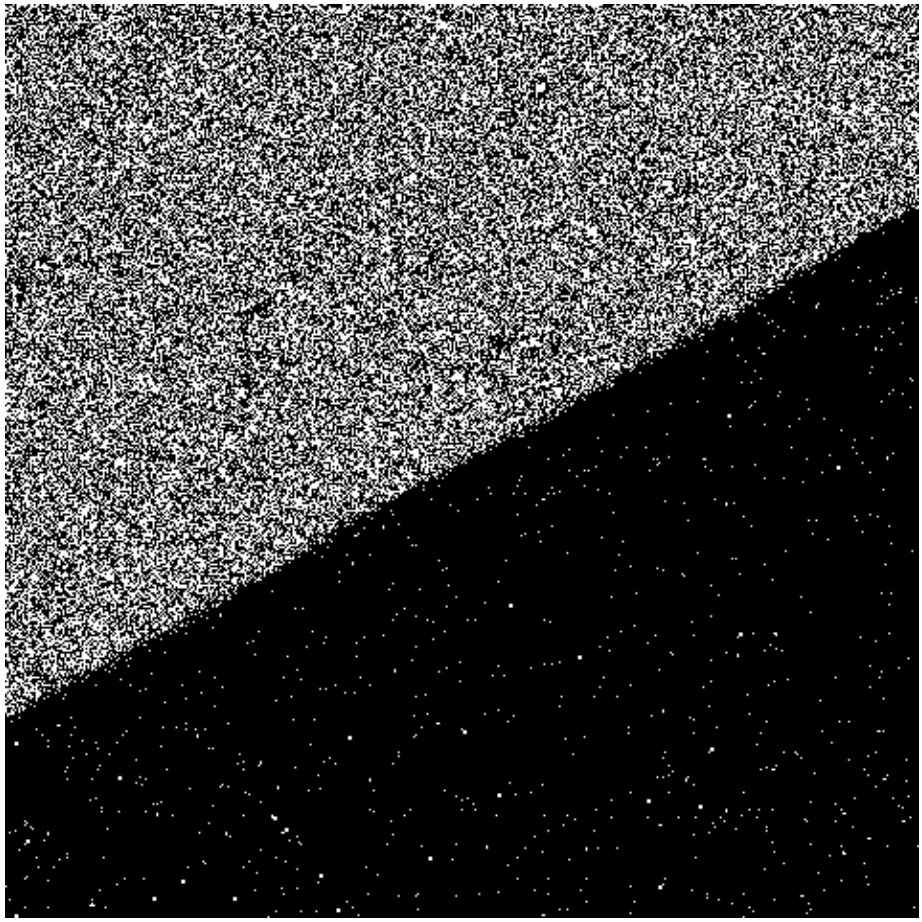

Figure 6.11: The same detail of the aluminum foil presented in figure 6.10 upscaled to a resolution of 370 nm. The upscaling is obtained by dividing each pixel of the imaging sensor into 9 subpixels and then assigning the detection of single positrons to one of the subpixels depending on the relative brightness of all the pixels that detected the positron. The technique requires a careful calibration of the thresholds used in the assignment of the event to different subpixels and is presented here as a preliminary attempt.

determined by the clock speed at which the sensor can transmit the pixel data and by the speed with which the SBC can process it.

6.3 Unmodified Sensor

In order to asses the need for modifying the image sensor at all, a control test was performed with a completely unmodified image sensor. It can be reasonably assumed that the color filter and microlens array combined amount to roughly 1 µm of material -

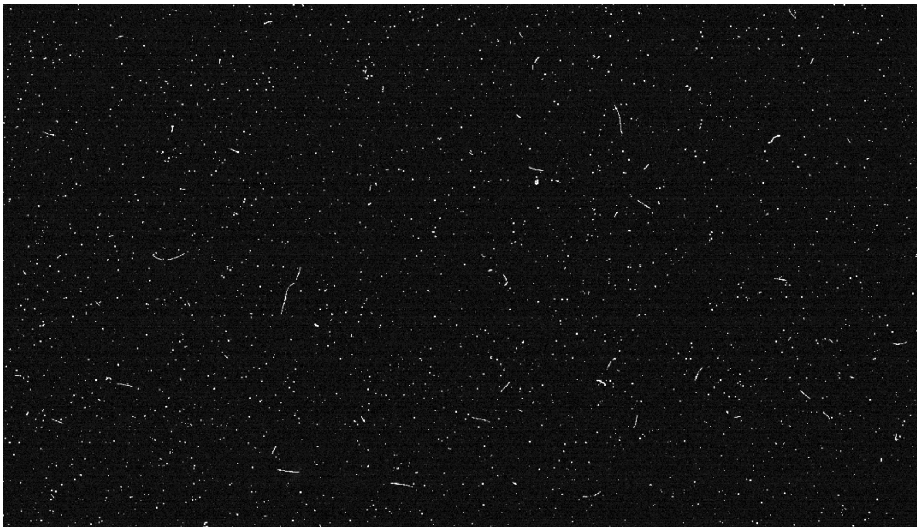

Figure 6.12: Section of an image acquired by an unmodified sensor. Numerous white streaks are visible across the frame with lengths varying between 10 and 70 μm. The most likely source for the white streaks are high energy ($>$ 60 keV) electrons resulting from the Compton scattering of the γs produced from positron annihilation.

most likely consisting of Diazonaphthoquinone(DNQ)-novolac - a photoresist based on low molecular weight polymers [36].

Exposing this sensor to the beam at an energy of 10 keV results in a weak but clearly distinguishable signal. It is likely that only very few positrons are able to penetrate far enough into the image sensor to reach the photosensitive area and create a signal. The images acquired using this setup did however exhibit randomly distributed white streaks having a length comprised between 10 and 70 µm that would only appear in the presence of the positron beam (Figure 6.12).

Upon further investigation and follow up experiments using an X-ray machine to expose a sensor to photons with an energy between 30 and 120 keV, deep Compton scattering of high energy γ-photons within the photosensitive area was identified as the most likely mechanism for this phenomenon. In this case, a 511 keV γ-photon produced by a positron annihilation reaction enters the Silicon substrate at a shallow angle and interacts with an electron transferring to it a sizeable portion of its energy. The high energy electron then travels through the substrate causing excitations in the pixels which are in turn registered as a signal by the sensor. The length of the streaks matches the average mean path in Silicon of an electron with kinetic energy comprised between 60 and 200 keV [48].

7 Conclusion and Outlook

In the present work, the feasibility of using commercial grade CMOS image sensors for low-energy positron detection was investigated. This would be achieved either indirectly – by first converting the impinging positron into visible light within a layer of high-efficiency phosphor – or without any intermediate conversion step, by directly implanting the particles into the pixel array. Both methods have been demonstrated to yield highly promising results both in terms of detection efficiency and spacial resolution.

By using a 70 µm thick layer of EJ-600 ZnS:Ag phosphor placed directly on top of the image sensor, the intensity and shape of a low-energy positron beam could be determined with a resolution of 10 µm within an exposure time of 10 seconds. The lower energy threshold below which the beam was now longer detectable was found to be around 3 keV. However, by considering the characteristics of the positron to photon conversion process within the phosphor as described in literature, it is strongly suspected that the absence of any signal below an energy of 3 keV was caused by poor beam focusing rather than by limitations in the detection system.

A procedure for chemically removing the color filter and microlens array was developed in order to modify commercial grade image sensors for the use in these experiments. After the procedure the sensors were able to detect individual positrons with an efficiency approaching 100% at 10 keV. The native spacial resolution with which these events could be recorded was confirmed to be 1.12 µm - surpassing the performance of any currently available MCP detectors. By statistically analysing multiple hours of acquired data, the spacial resolution could be improved even further, approaching 370 nm.

While this setup was not able to detect positrons at energies below 5.5 keV, an implantation depth scan of the sensor performed using DBS indicates that this cutoff could be caused by a previously undetected passivation layer shielding the photosensitive area of the image sensor. It is suspected that by removing this layer a CMOS sensor would be able to detect positrons at still lower energies.

The large market and great commercial interests that these sensors represent have enabled the development of a broad variety of specialized and highly capable image sensors based on CMOS technology. Based upon the results of this thesis, it is very likely that most of these products are either capable or could be easily adapted to detect low-energy positrons, enabling new and previously infeasible experiments. Large scale image sensors such as they are used in digital single-lens reflex (DSLR) cameras could be employed as beam monitors enabling very fast positional feedback over a large imaging area and therefore drastically reducing beam optimization times. Miniaturized high resolution sensors – such as the IMX219 used in this work – feature pixel sizes on the order of one micrometer and could provide highly resolved positional feedback thus enabling the optimisation of positron micro beams. The near unitary detection efficiency observed in the experiments of this thesis also suggests that CMOS image sensors could be used as single particle detectors. This aspect might be of particular interest when considering the adaptation of ultra high frame rate image sensors which are able to offer acquisition rates in excess of one million frames per second.

A particularly useful application of this technology might be the detection of positronium – a system consisting of an electron and positron bound together. While it is currently unclear whether or not this is at all possible, the potential applications in the extended field of antimatter research might very well warrant further investigation of this technology.

Acknowledgments

Firstly, I would like to express my gratitude towards Prof. Dr. Rudolf Neu for supervising this thesis and in doing so enabling me to pursue this fascinating topic. I also want to thank Vassily Burwitz and Lucian Mathes for their general expertise and guidance throughout this project and especially their support during the time of the positron experiment. Without them, none of the measurements presented here would have been possible. My gratefulness also extends to Maksym Melnyk whose help was instrumental and whose company made the many hours of sensor characterisation enjoyable.

Of course, none of this would have been possible without Dr. Francesco Guatieri, who not only envisioned this project but whose attitude, warmheartedness and humor made my time with the NEPOMUC group a great experience. I have many things to thank you for!

Bibliography

[1] Schmidt, Thomas. "Automated Positron Beam Adjustment and New Detector Read-Out at the Coincidence Doppler Broadening Spectrometer". Master Thesis. Technische Universität München, 2019.

[2] S. Aghion et al. "Positron bunching and electrostatic transport system for the production and emission of dense positronium clouds into vacuum". In: *Nucl. Instrum. Methods Phys. Res., Sect. B* 362 (2015), pp. 86–92. ISSN: 0168583X. DOI: 10.1016/j.nimb.2015.08.097.

[3] L.V Jørgensen et al. "A testing set-up for a micro-analysis positron beam facility". In: *Nucl. Instrum. Methods Phys. Res., Sect. A* 427.1-2 (1999), pp. 131–135. ISSN: 01689002. DOI: 10.1016/S0168-9002(98)01567-8.

[4] C. Hugenschmidt et al. "Positron Beam Characteristics at NEPOMUC Upgrade". In: *Journal of Physics: Conference Series* 505 (2014), p. 012029. DOI: 10.1088/1742-6596/505/1/012029.

[5] Thomas Gigl. "New Brightness Enhanced Positron Microbeam for Spatially Resolved Doppler Broadening Spectroscopy at NEPOMUC". Doctoral Dissertation. Technische Universität München, 2018.

[6] Joseph Ladislas Wiza. "Microchannel plate detectors". In: *Nucl. Instrum. Methods* 162.1-3 (1979), pp. 587–601. ISSN: 0029554X. DOI: 10.1016/0029-554X(79)90734-1.

[7] G. Vinelli et al. "Real-time monitoring of a positron beam using a microchannel plate in single-particle mode". In: *Journal of Instrumentation* 15.11 (2020), P11030–P11030. DOI: 10.1088/1748-0221/15/11/P11030.

[8] A. S. Tremsin et al. "Cross strip readouts for photon counting detectors with high spatial and temporal resolution". In: (2003), 996–1000 Vol.2. DOI: 10.1109/NSSMIC.2003.1351862.

[9] E. V. Stenson et al. “Positron-Induced Luminescence”. In: *Physical review letters* 120.14 (2018), p. 147401. DOI: 10.1103/PhysRevLett.120.147401.

[10] M. Dickmann et al. “Upgrade of the NEPOMUC Remoderator”. In: *Acta Physica Polonica A* 137.2 (2020), pp. 149–151. ISSN: 1898-794X. DOI: 10.12693/APhysPolA.137.149.

[11] Andreas Hänel et al. “Measuring night sky brightness: methods and challenges”. In: *Journal of Quantitative Spectroscopy and Radiative Transfer* 205 (2018), pp. 278–290. ISSN: 00224073. DOI: 10.1016/j.jqsrt.2017.09.008.

[12] Paul Adrien Maurice Dirac. “The quantum theory of the electron”. In: *Proc. R. Soc. London, Ser. A* 117.778 (1928), pp. 610–624. ISSN: 0950-1207. DOI: 10.1098/rspa.1928.0023.

[13] Paul Adrien Maurice Dirac. “Quantised singularities in the electromagnetic field”. In: *Proc. R. Soc. London, Ser. A* 133.821 (1931), pp. 60–72. ISSN: 0950-1207. DOI: 10.1098/rspa.1931.0130.

[14] David J. Griffiths. *Introduction to elementary particles*. 2., rev. ed., 5. reprint. Physics textbook. Weinheim: Wiley-VCH, 2011. ISBN: 978-3-527-40601-2.

[15] Peter J. Schultz and K. G. Lynn. “Interaction of positron beams with surfaces, thin films, and interfaces”. In: *Reviews of Modern Physics* 60.3 (1988), pp. 701–779. ISSN: 0034-6861. DOI: 10.1103/RevModPhys.60.701.

[16] A. van Veen et al. “Intense Positron Sources and their Applications”. In: *Materials Science Forum* 363-365 (2001), pp. 415–419. DOI: 10.4028/www.scientific.net/MSF.363-365.415.

[17] L. Liszkay et al. “Linac-based positron source and generation of a high density positronium cloud for the GBAR experiment”. In: *Journal of Physics: Conference Series* 443 (2013), p. 012006. DOI: 10.1088/1742-6596/443/1/012006.

[18] H. Schut et al. “Performance of an Intense Nuclear-Reactor Based Positron Beam”. In: *Materials Science Forum* 363-365 (2001), pp. 430–432. DOI: 10.4028/www.scientific.net/MSF.363-365.430.

[19] Christoph Hugenschmidt et al. “The NEPOMUC upgrade and advanced positron beam experiments”. In: *New Journal of Physics* 14.5 (2012), p. 055027. DOI: 10.1088/1367-2630/14/5/055027.

[20] D.W.O. Heddle. *Electrostatic Lens Systems, 2nd edition*. CRC Press, 2000. ISBN: 9781420034394. DOI: 10.1201/NOE0750306973.

[21] A. S. Tremsin, J. V. Vallerga, and O.H.W. Siegmund. “Overview of spatial and timing resolution of event counting detectors with Microchannel Plates”. In: *Nucl. Instrum. Methods Phys. Res., Sect. A* 949 (2020), p. 162768. ISSN: 01689002. DOI: 10.1016/j.nima.2019.162768.

[22] W. Plass et al. “High-resolution knife-edge laser beam profiling”. In: *Optics Communications* 134.1-6 (1997), pp. 21–24. ISSN: 00304018. DOI: 10.1016/S0030-4018(96)00527-5.

[23] Marcos A. C. de Araújo et al. “Measurement of Gaussian laser beam radius using the knife-edge technique: improvement on data analysis”. In: *Applied optics* 48.2 (2009), pp. 393–396. DOI: 10.1364/ao.48.000393.

[24] Nagayasu Oshima et al. “Development of Positron Microbeam in AIST”. In: *Materials Science Forum* 607 (2008), pp. 238–242. DOI: 10.4028/www.scientific.net/MSF.607.238.

[25] Barry Burke, Paul Jorden, and Paul Vu. “Overview Paper - CCD Technology”. In: *Scientific Detectors for Astronomy*, pp. 225–264. DOI: 10.1007/1-4020-4330-9_28.

[26] Moravian Instruments. *G2 CCD Camera User's Guide*. 2017.

[27] Alan Hoffman, Markus Loose, and Vyshnavi Suntharalingam. “CMOS Detector Technology”. In: *Experimental Astronomy* 19.1-3 (2006), pp. 111–134. ISSN: 0922-6435. DOI: 10.1007/s10686-005-9013-2.

[28] Rongzhu Zhang and Liping Lai. “Optical design of microlens array for CMOS image sensors”. In: *Design, Manufacturing, and Testing of Micro- and Nano-Optical Devices and Systems; and Smart Structures and Materials*. Ed. by Xiangang Luo et al. SPIE Proceedings. SPIE, 2016, p. 968502. DOI: 10.1117/12.2242261.

[29] Jr.Robert A. Maschal et al. “Review of Bayer pattern CFA demosaicing with new quality assessment algorithms”. In: *Infrared Imaging Systems: Design, Analysis, Modeling, and Testing XXI*. Ed. by Gerald C. Holst and Keith A. Krapels. SPIE Proceedings. SPIE, 2010, p. 766215. DOI: 10.1117/12.849314.

[30] OSRAM. *LB Q39G Datasheet*. 2022.

[31] Joachim Piprek. “Efficiency droop in nitride-based light-emitting diodes”. In: *physica status solidi (a)* 207.10 (2010), pp. 2217–2225. ISSN: 18626300. DOI: 10.1002/pssa.201026149.

[32] Leah Y. Kuritzky et al. “High wall-plug efficiency blue III-nitride LEDs designed for low current density operation”. In: *Optics express* 25.24 (2017), pp. 30696–30707. DOI: 10.1364/OE.25.030696.

[33] Shigeya Kimura et al. “Performance enhancement of blue light-emitting diodes with InGaN/GaN multi-quantum wells grown on Si substrates by inserting thin AlGaN interlayers”. In: *Journal of Applied Physics* 120.11 (2016), p. 113104. ISSN: 0021-8979. DOI: 10.1063/1.4962719.

[34] Michael Baumer, Christopher P. Davis, and Aaron Roodman. “Is Flat Fielding Safe for Precision CCD Astronomy?” In: *Publ. Astron. Soc. Pac.* 129.978 (2017), p. 084502. ISSN: 0004-6280. DOI: 10.1088/1538-3873/aa749f.

[35] Douglas Lanman, Ramesh Raskar, and Gabriel Taubin. *Modeling and Synthesis of Aperture Effects in Cameras*. 2008. DOI: 10.2312/COMPAESTH/COMPAESTH08/081-088.

[36] Harris R. Miller. “Color filter array for CCD and CMOS image sensors using a chemically amplified thermally cured pre-dyed positive-tone photoresist for 365-nm lithography”. In: *Advances in Resist Technology and Processing XVI*. Ed. by Will Conley. SPIE Proceedings. SPIE, 1999, p. 1083. DOI: 10.1117/12.350159.

[37] Thomas C. Wilkes et al. “Ultraviolet Imaging with Low Cost Smartphone Sensors: Development and Application of a Raspberry Pi-Based UV Camera”. In: *Sensors (Basel, Switzerland)* 16.10 (2016). DOI: 10.3390/s16101649.

[38] Environmental Protection Agency. *n-Methylpyrrolidone (NMP); Rulemaking under TSCA Section 6(a)(CASRN 872-50-4)*. 2020.

[39] SONY. *IMX219PQH5-C Datasheet*.

[40] Lucian Mathes. "Depth Resolved Doppler-Broadening Spectroscopy on Oxides Using a Table-Top Positron Beam". Master Thesis. Technische Universität München, 2020.

[41] Lucian Mathes. Ed. by Michael Berghold. 2022.

[42] Christian Edelmann. *Vakuumphysik: Grundlagen, Vakuumerzeugung und -messung, Anwendungen*. Heidelberg and Berlin: Spektrum Akad. Verl., 1998. ISBN: 978-3827400079.

[43] Paolo Chiggiato. *Outgassing properties of vacuum materials for particle accelerators*. 2020. DOI: 10.48550/ARXIV.2006.07124.

[44] Kilian Brenner. "In-operando positron beam experiments under extreme conditions". Bachelor Thesis. Technische Universität München, 2020.

[45] M. Y. Wang et al. "Dielectric and Electrical Insulation Properties of PTFE/PP for HTS Power Apparatus Application". In: pp. 621–624. DOI: 10.1109/ICD46958.2020.9342017.

[46] Julian Franz. "Implementation of a new Optimization Algorithm for Positron Beam Focusing". Bachelor Thesis. 2020.

[47] Ailing Wu, Yang Qiao, and Fengzheng Lv. "Study on the Electronic Structures of ZnS and Ag-doped ZnS from Density Functional Theory". In: DOI: 10.2991/icsmim-15.2016.169.

[48] Jerzy Dryzek and Paweł Horodek. "GEANT4 simulation of slow positron beam implantation profiles". In: *Nucl. Instrum. Methods Phys. Res., Sect. B* 266.18 (2008), pp. 4000–4009. ISSN: 0168583X. DOI: 10.1016/j.nimb.2008.06.033.